











Fundamental Reference AGN Monitoring Experiment (FRAMEx) I: Jumping Out of the Plane with the VLBA

TRAVIS C. FISCHER ^{1,2} NATHAN J. SECREST ² MEGAN C. JOHNSON ² BRYAN N. DORLAND ²
PHILLIP J. CIGAN ² LUIS C. FERNANDEZ ³ LUCAS R. HUNT ² MICHAEL KOSS ⁴ HENRIQUE R. SCHMITT ⁵ AND
NORBERT ZACHARIAS ²

¹*AURA for ESA, Space Telescope Science Institute, Baltimore, MD, USA, 3700 San Martin Drive, Baltimore, MD 21218, USA*

²*U.S. Naval Observatory, 3450 Massachusetts Ave NW, Washington, DC 20392-5420, USA*

³*Department of Physics and Astronomy, George Mason University, MS3F3, 4400 University Drive, Fairfax, VA 22030, USA*

⁴*Eureka Scientific, 2452 Delmer Street Suite 100, Oakland, CA 94602-3017, USA*

⁵*Naval Research Laboratory, Washington, DC 20375, USA*

ABSTRACT

We present the first results from the Fundamental Reference AGN Monitoring Experiment (FRAMEx), an observational campaign dedicated to understanding the physical processes that affect the apparent positions and morphologies of AGNs. In this work, we obtained simultaneous Swift X-ray Telescope (XRT) and Very Long Baseline Array (VLBA) radio observations for a snapshot campaign of 25 local AGNs that form a volume-complete sample with hard X-ray (14–195 keV) luminosities above 10^{42} erg s⁻¹, out to a distance of 40 Mpc. Despite achieving an observation depth of ~ 20 μ Jy, we find that 16 of 25 AGNs in our sample are not detected with the VLBA on milli-arcsecond (sub-parsec) scales, and the corresponding core radio luminosity upper limits are systematically below predictions from the Fundamental Plane of black hole activity. Using archival Jansky Very Large Array (VLA) radio measurements, our sample jumps back onto the Fundamental Plane, suggesting that extended radio emission is responsible for the apparent correlation between radio emission, X-ray emission, and black hole mass. We suggest that this discrepancy is likely due to extra-nuclear radio emission produced via interactions between the AGN and host environment. We compare VLBA observations of AGNs to VLA observations of nearby Galactic black holes (GBHs) and we find a mass-independent correlation between radio and X-ray luminosities of black holes of $L_{6\text{ cm}}/L_{2-10\text{ keV}} \sim 10^{-6}$, in line with predictions for coronal emission, but allowing for the possibility of truly radio silent AGNs.

Keywords: Radio astrometry (1337), Active galaxies (17), Radio active galactic nuclei (2134), X-ray active galactic nuclei (2035)

1. INTRODUCTION

Over the past several decades, supermassive black holes (SMBHs), which manifest as active galactic nuclei (AGNs), have gained profound importance to several fields of astrophysics. With the discovery of the $M_{\text{BH}} - \sigma$ relation (Ferrarese & Merritt 2000; Gebhardt et al. 2000) at the turn of the millennium, it became clear that SMBHs and their host galaxies co-evolve in some fashion, likely involving the mutual feeding of star formation and SMBH accretion, combined with “feed-

back” from the AGN into the surrounding interstellar medium via either the deposition of mechanical energy from a collimated jet, or radiative energy in the form of AGN winds (for an essential review of this topic, see Kormendy & Ho 2013). Similarly, the discovery of increasingly high-redshift quasars, such as the recent announcement of one powered by an $8 \times 10^8 M_{\odot}$ SMBH at a redshift of 7.54 (Bañados et al. 2018) when the universe was only a few hundred million years old, has raised serious questions about the formation mechanisms of black holes in the early universe (e.g., Volonteri 2010), and the distribution of quasars across the sky may even provide independent tests of our cosmological assumptions (e.g., Singal 2019, and references therein).

The nearly uniform distribution of quasars across the sky, combined with their negligible proper motions and significant luminosity at almost every wavelength, have additionally made them ideal objects with which to realize a quasi-inertial celestial reference frame, with the first quasar-based realization of the International Celestial Reference System (ICRS), the International Celestial Reference Frame (ICRF; Ma et al. 1998), being adopted at the same time as the discovery of SMBH-galaxy scaling relations. Successive refinements of the ICRF have improved both the density of these reference sources and their respective astrometric precision (ICRF2: Fey et al. 2015, and ICRF3: Charlot et al., in prep.). The ICRF has historically been a radio reference frame with quasar positions defined at 8.6 GHz. However, for the first time, the ICRF3 is now multi-wavelength with positions defined at 24 GHz (1.2 cm) and 32 GHz (0.9 cm) (Charlot et al., in prep.). If the ICRF is to be viewed as *the* fundamental reference frame for all astronomical positions and proper motions, there should be no significant disagreement between the radio positions of ICRF sources and their counterparts at other wavelengths. This has unfortunately not been the case, with evidence of the existence of significant optical-radio positional offsets being published soon after the release of ICRF1 (da Silva Neto et al. 2002), ICRF2 (Assafin et al. 2013; Orosz & Frey 2013; Zacharias & Zacharias 2014) and, along with the second data release of Gaia, ICRF3 (Makarov et al. 2017).

Earlier, pre-Gaia work hinted at an astrophysical nature to optical-radio offsets (Zacharias & Zacharias 2014), but the unprecedented astrometric precision of Gaia has put the astrophysical nature of these offsets on firm empirical ground (e.g., Harris et al. 2016; Kovalev et al. 2017; Petrov et al. 2019; Plavin et al. 2019). It is therefore imperative to understand how the physical phenomena associated with AGN activity, such as jets, intrinsic variability, variable obscuration, binary SMBHs, host galaxy morphology, etc. affect the apparent positions of AGNs and quasars across the electromagnetic spectrum.

Towards this goal, the U.S. Naval Observatory and its collaborators from partner institutions have begun the Fundamental Reference AGN Monitoring Experiment (FRAMEx), a research framework that includes the physical characterization and monitoring of AGN phenomena that may affect the apparent positions of AGNs at different wavelengths (see Dorland et al. (2020) for a more detailed overview of the FRAMEx collaboration and discussion of the relevant angular scales). While direct studies of the quasars that comprise the ICRF are an essential part of FRAMEx, their typical

redshifts of 1–2 correspond to a minimum distance separation of ~ 8 parsec at the milli-arcsecond (mas) resolution of very long baseline interferometry (VLBI) networks such as the Very Long Baseline Array (VLBA). The accretion regions of AGNs, which are typically confined to within ~ 1 parsec, are therefore much smaller in angular extent than what is typically observable, limiting research to AGN emission on large scales. It is therefore worthwhile to study more nearby AGNs, where mas-scale observations taken with facilities such as the VLBA can resolve features subtending only a few tenths of a parsec, providing a direct probe into the accretion physics of AGNs.

In this work, we present results from an initial snapshot survey of a volume-complete sample of 25 nearby (< 40 Mpc) AGNs, in which we obtained simultaneous observations with the VLBA and the Neil Gehrels Swift Observatory X-ray Telescope (XRT), as part of a long-term program to monitor the behavior of AGNs at sub-parsec scales. The simultaneity of these data mitigates the uncertainty introduced by variability that is inherent to studying AGNs on small physical scales, allowing a more robust assessment of the relationship between emission mechanisms at different wavelengths and energies. Our sample was selected from the Swift 105-month Burst Alert Telescope (BAT) catalog (Oh et al. 2018), enabling obscuration-independent selection of a statistically representative sample of nearby AGNs above some intrinsic luminosity limit.

The primary focus of this work is the relationship between the radio luminosity, X-ray luminosity, and black hole mass of AGNs, i.e. the Fundamental Plane of black hole activity (e.g., Merloni et al. 2003, hereafter the FP), which potentially serves as a parameter space unifying black hole accretion across all black hole masses, including Galactic black holes. We additionally explore the relationship between the core radio and X-ray luminosities of these AGNs more broadly, considering the potential bimodality between radio-loud and radio-quiet AGNs, as well as the prevalence of potentially truly radio-silent AGNs.

2. METHODOLOGY

2.1. Sample Selection

Our AGN sample was selected from the *Swift* BAT 105-month catalog (Oh et al. 2018). Because this catalog has a uniform flux limit ($\sim 8 \times 10^{-12}$ erg cm $^{-2}$ s $^{-1}$) across the sky, and hard X-rays (14–195 keV) reliably pick out bona-fide AGNs, even in the presence of heavy absorption ($N_H \lesssim 10^{24}$ cm $^{-2}$), constructing a volume-complete sample of AGNs above some luminosity threshold is straightforward. Additionally, AGNs from the

BAT catalog have extensive multi-wavelength coverage, and have the benefit of intense recent study (e.g., Trakhtenbrot et al. 2017; Shimizu et al. 2018; Powell et al. 2018; Bär et al. 2019).

We choose AGNs above a hard X-ray luminosity of 10^{42} erg s $^{-1}$, which corresponds to a distance limit of ~ 40 Mpc for a volume-complete sample using a flat Λ CDM cosmology with $H_0 = 70$ km s $^{-1}$ Mpc $^{-1}$ and $\Omega_M = 0.3$. This luminosity threshold was chosen to sample both moderate and high luminosity AGNs, and to provide a sample of AGNs close enough to give exquisite physical resolution on the AGN. Additionally, heavy, Compton-thick obscuration may cause lower luminosity AGNs beyond ~ 40 Mpc to be undetected even by BAT (e.g., LaMassa et al. 2019), biasing a sample extending further than 40 Mpc towards less obscured AGNs. At distances of less than 40 Mpc, the ~ 1 mas beam of the VLBA at 6 cm (C-band), samples physical scales of less than 0.2 pc, within the dusty obscuring medium (i.e., the “torus”) inferred to exist in most AGNs (e.g., Netzer 2015). Additionally, these physical scales correspond to light crossing times of only a few months, enabling relatively short-term studies of both luminosity and morphological variability.

Out of the 1105 AGNs in the 105-month BAT catalog, 43 are within the local volume defined here. For observability with the VLBA and other northern hemisphere facilities, we made an additional declination cut of $-30^\circ < \delta < +60^\circ$, leaving 25 targets. We illustrate our selection method in Figure 1 and provide a list of targets in Table 1.

Table 1 also presents reddening-corrected nuclear narrow H α luminosities, maximum expected star formation rates (SFR $_{\max}$) and maximum expected supernova rate (SNR $_{\max}$). The H α luminosities were calculated using nuclear emission line fluxes from Koss et al. (2017), except for NGC 1320 (de Grijp et al. 1992), NGC 2782 (Ho et al. 1997) and NGC 7465 (Moustakas & Kennicutt 2006). These flux measurements were obtained with small apertures (2'' to 4'') and corrected for reddening using the Calzetti et al. (2000) extinction law. These H α luminosities are used to determine the maximum expected supernova rate due to star formation, assuming that all of the narrow H α is due to star formation, providing an upper limit on any possible contamination of the nuclear AGN radio emission by SNe. We calculated SFR $_{\max}$ for our sample using the calibration from Kennicutt (1998). These values were converted to SNR $_{\max}$ using STARBURST99 continuous star formation models (Leitherer et al. 1999), assuming a Salpeter (1955) initial mass function and an age higher than 30 Myr where the supernova rate reaches a plateau. We find SNR $_{\max}$

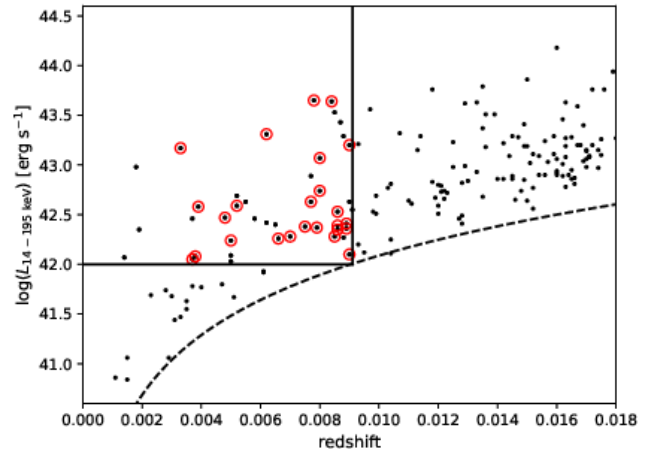


Figure 1. Redshift versus hard X-ray luminosity for AGNs from the 105-month Swift BAT catalog, showing the flux limit (dashed line) and our volume-complete cut (solid lines). Sources with declination between -30° and $+60^\circ$, circled in red, are observable with northern hemisphere facilities such as the VLBA and are the sample explored in this study.

ranging from 3.5×10^{-4} to 5.9×10^{-2} yr $^{-1}$, which allows us to conclude that the contribution from SNe to the nuclear radio emission is negligible.

We note that the distances we use are calculated from the sample redshifts, and the mean redshift of the sample is 0.007, so the effect of peculiar motions on the cosmological distance estimates may be significant. To estimate this, we retrieved redshift-independent distances for our sample using the NASA Extragalactic Database (NED),¹ and calculated the amount of additional, intrinsic uncertainty that is required for the luminosity using the cosmological distance estimate to be consistent with the luminosity using the redshift-independent distance, in a reduced χ^2 sense. We found 13 unique methods used to estimate the redshift-independent distances of our sample: ring diameter (Pedreros & Madore 1981), Faber-Jackson and “tertiary” methods (e.g., de Vaucouleurs & Olson 1984), Tully estimate distances (Tully & Fisher 1988), CO ring diameter (Sofue 1991), D-sigma and the Infrared Astronomical Satellite standard candle (Willick et al. 1997), the “fundamental plane” of early-type galaxies (unrelated to the fundamental plane of black hole activity; e.g., Blakeslee et al. 2001) look-alike (“sosie”) galaxies (Terry et al. 2002), surface brightness fluctuations (e.g., Tully et al. 2013), AGN time lags (e.g., Hönig et al. 2014), Tully-Fisher (e.g., Tully et al. 2016), and type Ia supernovae (e.g., Koshida et al. 2017). We found the value the intrinsic uncertainty to be 0.31 dex.

¹ <https://ned.ipac.caltech.edu>

Target	R.A. (ICRS) (deg)	Decl. (ICRS) (deg)	Type	Redshift	Distance (Mpc)	$\log(M_{\text{BH}})$ [M_{\odot}]	$\log(L_{\text{H}\alpha})$ [erg s^{-1}]	SFR_{max} ($M_{\odot} \text{ yr}^{-1}$)	SNR_{max} (yr^{-1})
NGC 1052	40.2699884	-8.25576190	Sy2	0.0050	21.5	8.67	40.15	0.11	2.2×10^{-3}
NGC 1068	40.6696342	-0.01323785	Sy2	0.0038	16.3	6.93	41.34	1.74	3.5×10^{-2}
NGC 1320	51.2028681	-3.04226840	Sy2	0.0089	38.4	7.96	40.49	0.24	4.9×10^{-3}
NGC 2110	88.0473918	-7.45625094	Sy2	0.0078	33.6	9.38	40.68	0.38	7.5×10^{-3}
NGC 2782	138.5212787	+40.11369022	Sy2	0.0085	36.6	6.07	41.51	2.62	5.2×10^{-2}
IC 2461	139.9914308	+37.19100007	Sy2	0.0075	32.3	7.27	39.40	0.02	3.9×10^{-4}
NGC 2992	146.4247756	-14.32626689	Sy1	0.0077	33.2	8.33	40.11	0.10	2.0×10^{-3}
NGC 3081	149.8731005	-22.82631476	Sy2	0.0080	34.5	7.74	40.97	0.74	1.5×10^{-2}
NGC 3089	149.9028701	-28.33129443	Sy2?	0.0090	38.8	6.55
NGC 3079	150.4908469	+55.67979744	Sy2	0.0037	15.9	6.38	40.04	0.09	1.7×10^{-3}
NGC 3227	155.8774015	+19.86505766	Sy1	0.0039	16.8	6.77	40.78	0.48	9.6×10^{-3}
NGC 3786	174.9271391	+31.90942732	Sy2	0.0089	38.4	7.48	40.73	0.42	8.4×10^{-3}
NGC 4151	182.6357547	+39.40584860	Sy1	0.0033	14.2	7.55	41.21	1.27	2.5×10^{-2}
NGC 4180	183.2626924	+7.03891255	LINER	0.0070	30.1	7.63
NGC 4235	184.2911678	+7.19157597	Sy1	0.0080	34.5	7.55	40.94	0.68	1.4×10^{-2}
NGC 4388	186.4449188	+12.66215153	Sy2	0.0084	36.2	6.94	41.57	2.93	5.9×10^{-2}
NGC 4593	189.9143400	-5.34417010	Sy1	0.0090	38.8	6.88	40.65	0.35	7.0×10^{-3}
NGC 5290	206.3297085	+41.71241871	Sy2	0.0086	37.1	7.78	40.12	0.10	2.1×10^{-3}
NGC 5506	213.3119888	-3.20768334	Sy1.9	0.0062	26.7	6.96	41.18	1.19	2.4×10^{-2}
NGC 5899	228.7634964	+42.04991289	Sy2	0.0086	37.1	7.69	41.19	1.23	2.5×10^{-2}
NGC 6814	295.6690092	-10.32345792	Sy1	0.0052	22.4	7.04	39.35	0.02	3.5×10^{-4}
NGC 7314	338.9424567	-26.05043820	Sy1.9	0.0048	20.6	6.76	39.68	0.04	7.5×10^{-4}
NGC 7378	341.9486864	-11.81658744	Sy2	0.0086	37.1	4.93
NGC 7465	345.5039963	+15.96477472	Sy2	0.0066	28.4	6.54	40.44	0.22	4.3×10^{-3}
NGC 7479	346.2359605	+12.32295297	Sy2	0.0079	34.0	7.61	40.02	0.08	1.7×10^{-3}

Table 1. FRAMEx Volume-complete Sample

Using the Merloni et al. (2003) FP relation and propagation of uncertainty, however, the scatter induced by the absolute luminosity uncertainty is only 0.19 dex. Moreover, this source of uncertainty also affected the sources studied by Merloni et al. (2003, see their Section 3.1), and makes only a minor contribution to the overall dispersion in the FP (see Section 6.1 in Merloni et al. 2003). We therefore use the cosmological distances for our sample, which are more generally available than redshift-independent distances.

2.2. VLBA Observations

In order to estimate the required integration time of our sample, we used the FP given in (Merloni et al. 2003), a $10^6 M_{\odot}$ black hole with a hard X-ray luminosity of $10^{42} \text{ erg s}^{-1}$ would result in a 6 cm (6 GHz) radio peak luminosity of approximately $10^{36} \text{ erg s}^{-1}$. This yields a flux of $\sim 100 \mu\text{Jy beam}^{-1}$ at the maximum distance of ~ 40 Mpc for our sample. To ensure our targets are robustly detected, we designed our observations to achieve

a signal-to-noise (S/N) ratio of 5, or a root mean square (RMS) noise of $\sim 20 \mu\text{Jy beam}^{-1}$. Using the European VLBI Network’s online calculator,² we determined that one hour of on-source integration time produces a 1σ image thermal noise of $23 \mu\text{Jy beam}^{-1}$.

To ensure accurate VLBA pointing for all of our targets, which is necessary due to the small effective field of view (a few arcsec) in the C-band, we used the most accurate AGN positions of our targets. For 17 of our objects we determined the AGN positions from archival VLA A-array configuration observations in the X-band (~ 9 GHz), which provided a pointing accuracy of roughly 50 mas. Two of our targets had archival C-band (~ 5 GHz) VLA data in the A-array and B-array configurations for an a priori positional accuracy of 80 mas and 370 mas, respectively. The remaining 6 objects did not have any archival VLA data with the re-

² <http://old.evlbi.org/cgi-bin/EVNcalc>

quired positional accuracy for VLBA pointing and thus, we used the Pan-STARRS y -band data for 5 galaxies providing a pointing accuracy of ~ 300 mas and for 1 galaxy we used the Chandra X-ray position, which has an a priori positional accuracy of 500 mas. These AGN positions are well within the desired pointing accuracy for the VLBA and provide high confidence for ensuring we imaged the AGN at our sub-parsec spatial scale should it exist.

As one of the primary goals of these VLBA snapshot observations is to produce high fidelity images, we devised an observing strategy to maximize uv sky coverage by dividing the 25 targets into bins of similar right ascension. This produced six groups, each containing three to five sources. We observed each target in a given bin for 20 minutes before slewing to the next target in the bin. We continued in this fashion, cycling back through each of the targets three times to reach a full, one hour on-source total integration time. In this manner, we were able to track parallactic angles three to five times longer than if we observed each source independently, thereby producing a better-sampled uv plane. We used phase referencing in order to accurately constrain the phases and ultimately the positions of each target. Table 2 lists the observing parameters including, the center frequency, restoring beam parameters as measured in the plane of the sky and then rotated by the beam position angle, RMS noise of the cleaned image, and the phase calibrator name and position. For each observation, we used a data rate of 2048 Mbps with 2 bit sampling in a single right circular polarization with four intermediate frequency (IF) windows each with a width of 128 MHz and 512 channels. This recording setup permitted a bandwidth smearing limit of $\sim 22''$ and a time smearing limit of $\sim 5''$. The positions for sources are known to within the error of the positions of the phase reference calibrators, which have all come from the ICRF3 (Charlot et al., in prep.) and have a median formal error of $\sigma_\alpha = 6.4 \mu\text{as}$, $\sigma_\delta = 137.3 \mu\text{as}$.

2.2.1. Data Calibration

We calibrated our VLBA data using the National Radio Astronomy Observatory (NRAO) Astronomical Image Processing System (AIPS; van Moorsel et al. 1996), release 31DEC19. We loaded the data with a calibration (CL) table interval of 0.1 minutes. We loaded in each galaxy with its corresponding phase calibrator independently from the other sources and phase calibrators in the datasets such that all calibrations could be done to one target-phase calibrator pair at a time. We performed all calibrations to the phase calibrator. Using the VLBAUTIL module, we corrected for the following:

ionosphere delay, Earth orientation, correlator sampler threshold errors, instrument delay, bandpass, amplitude, and parallactic angle. Next, we flagged the data on both the target and the phase calibrator, one source at a time using the EDITR task to remove any bad data and radio frequency interference (RFI). Then, we solved for complex amplitudes and phases for the phase calibrator using FRINGE and applied the solutions from the phase calibrator to the source by using a two-point interpolation. The calibrations were then applied using the task SPLIT. After these standard AIPS calibration procedures were completed, we moved onto the imaging process.

2.2.2. Imaging

To image each target, we used the AIPS imaging task IMAGR. For each target we used similar input parameters including a Briggs weighting with `robust` = 5.0 for a natural weighting in order to maximize sensitivity and a pixel size of 0.8 mas, which Nyquist-samples the synthesized beam. We took extreme care in determining the RMS of our VLBA data by initially determining the RMS from a “dirty image,” which is made when the number of iterations is set to zero for an initial iteration of CLEAN. Next, we deconvolved the point spread function using no more than 500 iterations of CLEAN to derive the best estimate for the true RMS noise of each image (see Table 2). We interactively placed clean boxes around all point source emission and interactively cleaned until a thermal noise limited image was made. For several of our observations, there were significant amounts of RFI and some antennas required complete flagging altogether. For example, for all sources, the Kitt Peak VLBA antenna suffered a pointing error due to a software bug and thus, required flagging altogether for the duration of our observations. In the observing session that included NGC 4151, NGC 4180, NGC 4235, NGC 4388, and NGC 4593, we had to flag an additional two antennas due to RFI and other issues in the data. For these reasons, the RMS values for these targets presented in Table 2 are above the theoretical RMS by factors of 4-5.

For the imaging procedure, we started with a field of view of 512 pixels per side, which we increased systematically to search for point source emission, while being mindful not to introduce effects from bandwidth or time smearing. For sources where we did not detect a point source, we imaged out to a radius of $\sim 1''.5$ from the phase center of the source positions. One of our detected targets, NGC 5290, had a position offset of $+0''.35$, $-0''.2$ in R.A. and Decl., respectively, from the a priori position as determined from the Pan-STARRS y -band data.

Target	Frequency (GHz)	Restoring Beam ($\alpha \times \delta$; mas)	Beam angle (deg)	RMS ($\mu\text{Jy bm}^{-1}$)	Calibrator IERS Name	R.A. (deg(μs))	Decl. (deg(μas))
NGC 1052	5.873692	3.83 \times 1.49	8.4	4242.0	0240-060	40.801956142(4.78)	-5.8486932(137.3)
NGC 1068	5.858862	3.48 \times 1.60	14.7	21.7	0237-027	39.939467802(2.09)	-2.57803183(31.9)
NGC 1320	5.867662	7.46 \times 2.02	-15.9	39.1	0319-056	50.499459824(8.17)	-5.4367857(222.2)
NGC 2110	5.861240	3.37 \times 1.51	5.3	162.0	0551-086	88.42454680(13.99)	-8.6671937(157.8)
NGC 2782	5.867662	2.82 \times 2.23	18.1	33.0	0913+391	139.203769060(7.04)	38.9078184(115.6)
IC 2461	5.870108	2.92 \times 2.20	17.0	35.3	0922+364	141.466047268(6.73)	36.2099096(118.2)
NGC 2992	5.869068	6.68 \times 2.52	-13.7	105.1	0938-133	145.260622829(6.07)	-13.5974958(193.9)
NGC 3081	5.874081	6.80 \times 3.23	-7.0	43.7	1004-217	151.693390348(4.80)	-21.9890028(109.5)
NGC 3089	5.873428	7.91 \times 3.36	2.9	60.1	1008-285	152.772989020(7.74)	-28.7945604(246.8)
NGC 3079	5.887221	3.31 \times 1.78	17.9	441.6	0954+556	149.40910265(63.41)	55.38271342(38.3)
NGC 3227	5.874904	5.13 \times 1.77	-11.9	48.3	1022+194	156.186706652(2.61)	19.20567097(41.3)
NGC 3786	5.878159	3.25 \times 1.70	21.6	47.9	1133+344	174.113933109(8.91)	34.1276345(181.3)
NGC 4151	5.855409	3.13 \times 1.78	42.4	175.1	1204+399	181.654389055(8.75)	39.6843742(132.2)
NGC 4180	5.868327	6.92 \times 1.55	-4.2	76.3	1212+087	183.749638201(8.64)	8.4895883(191.2)
NGC 4235	5.906512	3.36 \times 1.48	-7.6	106.4	1212+087	183.749638201(8.64)	8.4895883(191.2)
NGC 4388	5.868400	2.76 \times 1.60	13.0	107.9	1222+131	186.265597247(4.1)	12.8869831(138)
NGC 4593	5.869410	6.93 \times 1.52	-6.7	145.3	1245-062	192.095731923(4.98)	-6.5360605(154.7)
NGC 5290	5.883406	3.69 \times 2.02	-19.9	61.8	1357+404	209.908726091(7.73)	40.1939585(120.2)
NGC 5506	5.872330	5.36 \times 1.78	-16.9	352.9	1402-012	211.191231047(5.89)	-1.50609643(93.6)
NGC 5899	5.869410	6.93 \times 1.52	-6.7	42.1	1505+428	226.721007704(6.32)	42.65639874(79)
NGC 6814	5.873225	5.88 \times 2.08	-11.6	50.0	1937-101	294.988569046(4.17)	-10.04486683(98.1)
NGC 7314	5.876574	7.68 \times 3.73	3.9	81.5	2240-260	340.860036591(6.44)	-25.7418576(189.9)
NGC 7378	5.865883	6.82 \times 2.38	-12.3	46.7	2243-123	341.575966543(2.11)	-12.11424378(33.5)
NGC 7465	5.876460	4.30 \times 2.13	-15.9	47.4	2258+166	345.179129648(7.01)	16.9206644(148.4)
NGC 7479	5.872223	4.43 \times 2.04	-17.1	43.5	2307+106	347.618823901(2.5)	10.92519353(41.8)

Table 2. VLBA Observations

Name	R.A. (deg)	Decl. (deg)	F_{peak} (mJy bm^{-1})	$\text{Log } F_{peak}^a$ ($\times 10^{-16} \text{ erg s}^{-1} \text{ cm}^{-2}$)	$\text{Log } L_{peak}$ (erg s^{-1})	S_{int}^a (mJy)
NGC 1052	40.2699939	-8.2557642	745 \pm 15	437 \pm 8.8	39.38	1269 \pm 14
NGC 1068	40.6696212	-0.0133181	0.198 \pm 0.016	0.116 \pm 0.0094	35.57	2.37 \pm 0.19
NGC 2110	88.0474013	-7.4562554	6.89 \pm 0.07	4.04 \pm 0.041	37.73	11.15 \pm 0.17
NGC 2992	146.4247680	-14.3262771	1.01 \pm 0.04	0.592 \pm 0.023	36.89	1.29 \pm 0.10
NGC 3079	150.4908485	55.6797891	9.95 \pm 0.29	5.84 \pm 0.17	37.24	27.02 \pm 0.96
NGC 4151	182.6357579	39.4058501	2.94 \pm 0.14	1.73 \pm 0.082	36.62	11.61 \pm 0.66
NGC 4235	184.2911738	7.1915751	2.56 \pm 0.023	1.50 \pm 0.013	37.33	3.11 \pm 0.049
NGC 5290	206.3298364	41.7123508	2.32 \pm 0.051	1.36 \pm 0.029	37.35	6.49 \pm 0.19
NGC 5506	213.3119889	-3.2076829	21.90 \pm 0.14	12.9 \pm 0.0082	38.04	29.67 \pm 0.32

^aPeak flux values, corresponding to the observations in Table 2, derived from CASA's 2-D Gaussian model fitting algorithm and integrated flux densities are determined from flux measured within the 3σ outer contour shown in Figure 2.

Table 3. VLBA Measurements

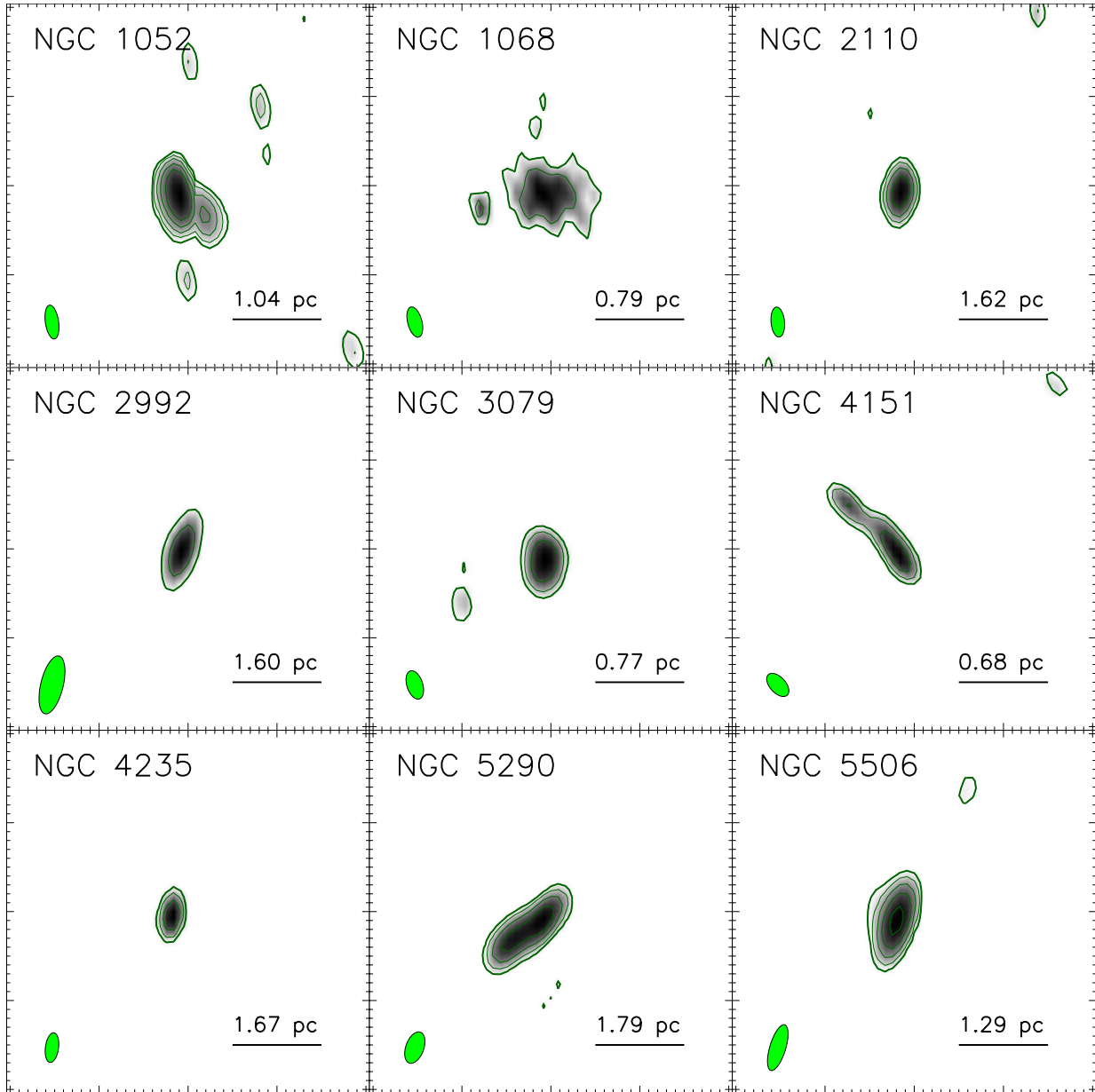


Figure 2. 5 GHz (C-band) parsec-scale radio morphologies for the VLBA detected sources in our sample. Thick, outer contours represent a 3σ flux limit above RMS, with interior contours increasing in powers of $3\sigma \times 2^n$. Green ellipses to the lower left of each flux distribution represent the synthesized beam size for that observation. Scale bars represent an angular size of 10 mas.

Thus, we applied this R.A. and Decl. offset in the imaging process in order to center the source in the field of view.

Once we had produced initial images, we then proceeded with self-calibration for the nine objects that we detected. Our self-calibration procedure utilized the AIPS task CALIB and we started by self-calibrating on phase using the initial input image. Self-calibration is only viable for high S/N detections and thus, we are only able to apply this technique to the nine objects for which we achieved an S/N of >15 . This is an iterative process, running CALIB and IMAGR to create new images from the preceding calibrated uv data files. We repeated this process for several cycles, usually between three or four, until there was little to no improvement in the RMS noise. Once this was achieved, we then continued self-calibration by calibrating both the amplitudes and phases. After a few more iterations, our images converged and the RMS noise in the final resulting image no longer improved. Because we utilized phase referencing, our absolute source positions were preserved throughout the self-calibration process. For NGC 1068, however, self-calibration was not applied as this source suffers from severe short spacing artifacts and requires a multi-scale imaging technique. We used four spatial scales for our multi-scale imaging algorithm at 0, 2, 4, and 8 times the restoring beam and we imaged 2048×2048 pixels. The final images for our nine detected nuclear AGN sources are presented in Figure 2.

2.3. VLA Observations

We also include archival images of our sample from the NRAO VLA Archive Survey (NVAS)³, when available, at ~ 4.89 GHz. Largely taken in A-Configuration, we include these datasets in our analysis to compare how peak fluxes, of ostensibly core radio AGN emission, may in fact differ depending on different resolutions. Of the 25 targets in our sample, 19 possessed relevant observations in the archive.

2.4. Radio Analysis

The NRAO Common Astronomical Software Applications (CASA; McMullin et al. 2007)⁴ was used to analyze each image in our VLBA and VLA observations. Using the VIEWER command in CASA, we utilized the two-dimensional fitting application to determine both peak flux and integrated flux densities for the 9 detected sources in our VLBA observations and the entirety of the 19 sources observed by the VLA. Peak flux values were

measured directly from the image and integrated values were measured by enclosing all nuclear flux greater than 3σ or 5σ for VLBA and VLA measurements, respectively. The VLA flux distribution in NGC 1068 contains several discrete regions that are not connected to the nuclear emitting region that were also included in its integrated flux density measurement. Table 3 shows the flux parameters for all nine detections and Table 4 shows the peak flux and integrated flux densities for the VLA observations.

2.5. Swift XRT Observations

We obtained Target of Opportunity (ToO) observations (PI: N. Secrest) of 20 out of 25 of our sample with the Neil Gehrels Swift Observatory X-ray Telescope (XRT; Burrows et al. 2003; Hill et al. 2004; Burrows et al. 2005), which has a PSF with a half-power diameter of $18''$ and FWHM of $7''$ at 1.5 keV, and a positional accuracy of $3''$. These observations were simultaneous with our VLBA observations to obtain a simultaneous snapshot of the radio and X-ray properties of our volume-complete sample of AGNs, as is generally warranted when comparing the radio and X-ray properties of AGNs (e.g., Merloni et al. 2003; Gültekin et al. 2009). Three of the five objects we did not acquire observations of were visibility-constrained and the ToOs for the remaining objects, IC 2451 and NGC 2992, were approved but not executed. We requested 1.8 ks integrations for all ToOs, with one ToO set up in Windowed Timing (WT) mode to avoid possible pileup and the remaining ToOs in Photon Counting (PC) mode following the recommendation of the Science Operations Team. Finally, although our ToO observation for NGC 2992 was not executed, a separate XRT observation of NGC 2992 was taken during the requested time, in PC mode, which we include with our data.

We generated X-ray spectra for our data using the online XRT product generator (Evans et al. 2009),⁵ allowing the routine to center the X-ray sources within the default $1'$ search radius. For objects where centroiding failed due to faintness, such as NGC 4180, we turned off centroiding and set the extraction coordinates to the target coordinates used for the ToO, which were the same as the VLBA targeting coordinates.

2.6. X-ray Analysis

Similar to the procedure outlined in Ricci et al. (2017), we carried out a joint X-ray spectral analysis by combining the contemporaneous XRT data with the time-averaged 105-month BAT data, and fitting models of

³ <http://archive.nrao.edu/nvas>

⁴ <https://casa.nrao.edu>

⁵ https://www.swift.ac.uk/user_objects/

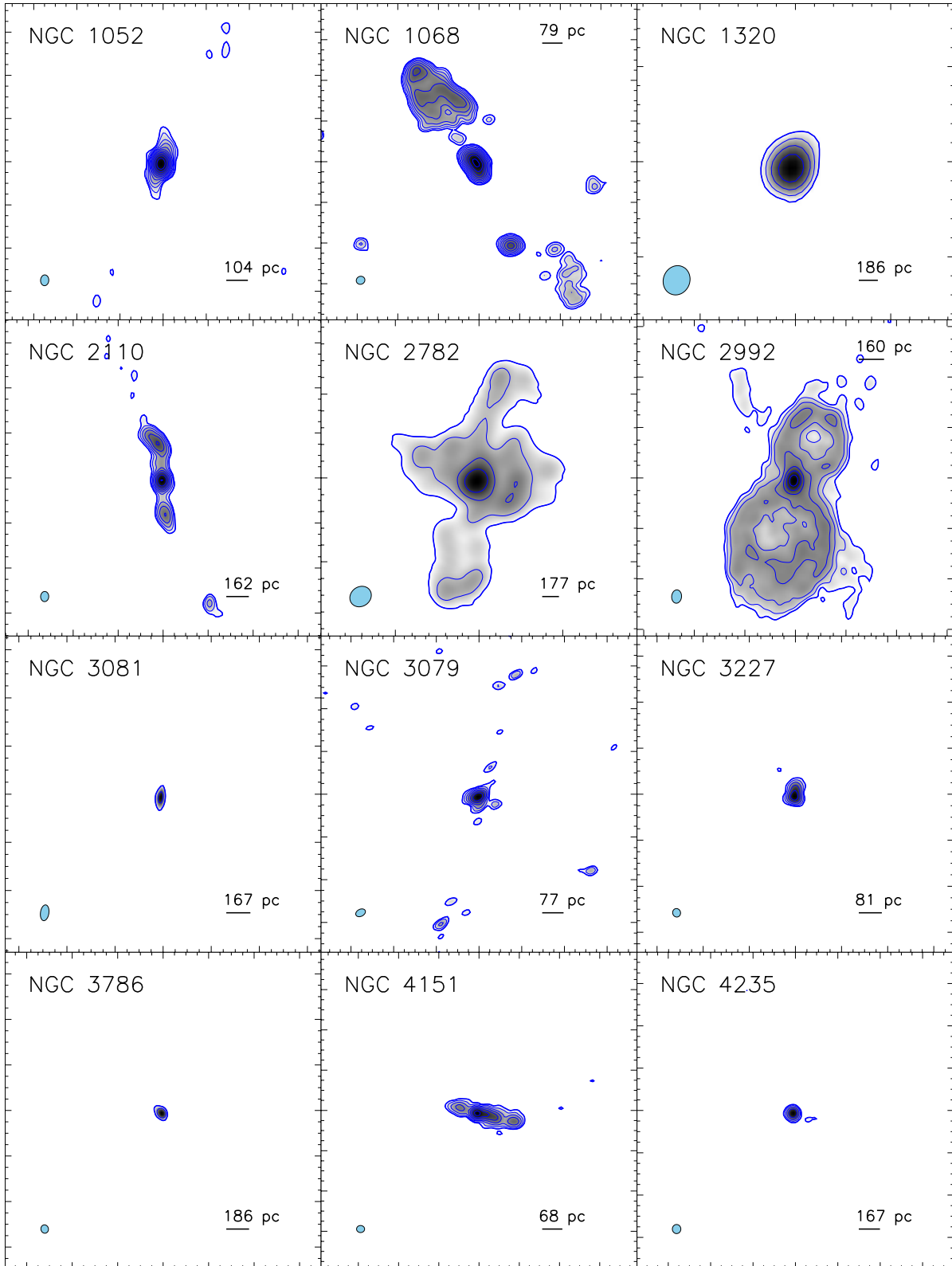
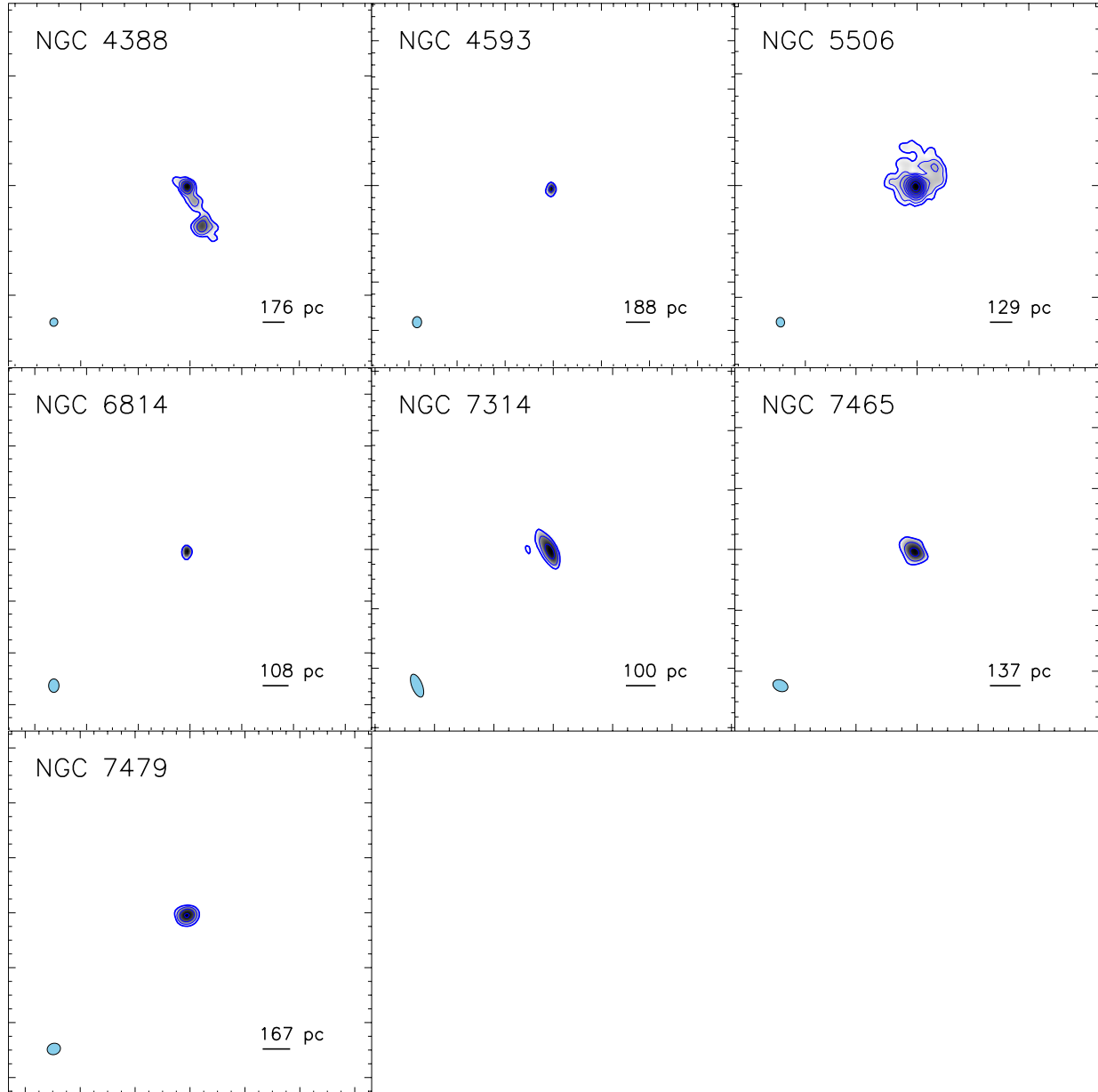


Figure 3. C-band (4.9 GHz) hundred-parsec-scale radio morphologies for the VLA observed sources in our sample. Thick, outer contours represent a 5σ flux limit above RMS, with interior contours increasing in powers of $5\sigma \times 2^n$. Blue ellipses to the lower left of each flux distribution represent the synthesized beam size for that observation. Scale bars represent an angular size of $1''$.

**Figure 3.** (*cont.*)

Name	Frequency (GHz)	VLA Config.	Restoring Beam ($\alpha \times \delta$; $''$)	Beam Angle (deg)	RMS ($\mu\text{Jy bm}^{-1}$)	F_{peak} (mJy bm^{-1})	F_{peak} ($\text{erg s}^{-1} \text{cm}^{-2}$)	$\text{Log } L_{peak}$ (erg s^{-1})	S_{int}^a (mJy)	$F_{peak} /$ VLBA $_{RMS}$
VLBA Detected Sources										
NGC 1052	4.86	A	0.50×0.38	−3°2	177.0	1808	8.79×10^{-14}	39.67	1889	142.1
NGC 1068	4.86	A	0.43×0.39	−67°1	80.6	252	1.22×10^{-14}	38.59	980	3871.0
NGC 2110	4.99	A	0.45×0.36	−2°6	78.9	53.5	2.67×10^{-15}	38.55	108	110.1
NGC 2992	4.86	A	0.53×0.39	−5°2	18.3	8.0	3.88×10^{-16}	37.71	57.7	25.3
NGC 3079	4.99	A	0.48×0.33	−63°5	162.0	58.4	2.91×10^{-15}	37.95	89.0	44.1
NGC 4151	4.99	A	0.40×0.35	88°9	90.4	38.2	1.91×10^{-15}	37.66	102.0	72.8
NGC 4235	4.86	A	0.43×0.40	0°4	59.7	4.6	2.25×10^{-16}	37.50	5.17	14.5
NGC 5290	–	–	–	–	–	–	–	–	–	–
NGC 5506	4.86	A	0.43×0.37	12°2	103.0	102.	4.96×10^{-15}	38.63	154	96.3
VLBA Non-detections										
NGC 1320	4.86	B	1.56×1.39	−21°8	22.9	1.65	8.04×10^{-17}	37.15	1.92	20.9
NGC 2782	4.86	B	1.34×1.16	−54°4	60.3	1.50	7.29×10^{-17}	37.07	2.58	17.3
IC 2461	–	–	–	–	–	–	–	–	–	–
NGC 3081	4.86	A	0.66×0.35	−8°2	54.5	0.500	2.43×10^{-17}	36.54	0.502	4.5
NGC 3089	–	–	–	–	–	–	–	–	–	–
NGC 3227	4.86	A	0.37×0.34	18°2	91.9	10.8	5.24×10^{-16}	37.25	22.2	88.0
NGC 3786	4.86	A	0.37×0.33	14°8	87.6	1.70	8.26×10^{-17}	37.16	2.51	13.8
NGC 4180	–	–	–	–	–	–	–	–	–	–
NGC 4388	4.86	A	0.38×0.36	−28°5	44.8	3.17	1.54×10^{-16}	37.38	9.26	19.7
NGC 4593	4.86	A	0.46×0.38	−2°0	94.0	1.15	5.59×10^{-17}	37.00	1.23	10.3
NGC 5899	–	–	–	–	–	–	–	–	–	–
NGC 6814	4.86	A	0.52×0.4	−0°6	135.0	1.16	5.64×10^{-17}	36.52	1.40	8.9
NGC 7314	4.86	A	0.82×0.35	22°0	65.9	1.72	8.36×10^{-17}	36.53	2.00	8.3
NGC 7378	–	–	–	–	–	–	–	–	–	–
NGC 7465	4.86	A	0.51×0.37	66°6	48.6	1.21	5.88×10^{-17}	36.76	1.61	10.8
NGC 7479	4.86	A	0.49×0.41	−72°6	51.4	2.43	1.18×10^{-16}	37.22	2.46	18.7

^a 5σ contour

Table 4. VLA archival observations and measurements

increasing complexity. We fit the X-ray spectra using XSPEC (Arnaud 1996), version 12.10.1f, using **phabs** to model both intrinsic and Galactic absorption for consistency with the MYTorus model (Murphy & Yaqoob 2009) that we use for Compton-thick sources, which requires the Anders & Grevesse (1989) abundances and the Verner et al. (1996) photo-ionization cross-sections. For Galactic absorption, we use the Swift online Galactic N_{H} tool,⁶ which uses the method of Willingale et al. (2013).

We began by fitting a single power-law component **pow**, allowing the normalizations to vary between the XRT and BAT data to account for variability. If soft X-ray absorption is clearly present, we appended a **phabs**

component to account for intrinsic absorption, again allowing the normalizations to vary. For some sources, a soft excess is present. This we fit with either a blackbody component (**bb**) or an additional, non-absorbed power-law component. For sources in which the best-fit N_{H} approached Compton-thick levels ($> 10^{24} \text{cm}^{-2}$), we used MYTorus. We note that because of the $\sim 10 \text{keV}$ coverage gap between the XRT and BAT data, for some sources we relied on the spectral curvature in the BAT data to determine if a source is Compton-thick (e.g., Koss et al. 2016). In all cases, the 2–10 keV flux we calculate is rest-frame, corrected for absorption, and from the intrinsic power-law component only. For Compton-thick sources, the scattered component may dominate the high-energy continuum (e.g., Murphy & Yaqoob 2009), necessitating the use of a physical model such as MYTorus to infer the strength of the intrinsic power-

⁶ <https://www.swift.ac.uk/analysis/nhtot/>

Target	Swift Target ID	R.A. deg	Decl. deg	Mode	UTC Start	UTC Stop	Obs. Time second
NGC 2110	35459	88.0473918	-7.45625094	WT	4/12/19 17:20	4/13/19 00:00	1525
NGC 2782	37237	138.5212787	40.11369022	PC	4/14/19 23:09	4/16/19 07:53	1670
NGC 2992	35344	146.4247756	-14.32626689	PC	4/14/19 23:09	4/15/19 07:53	1505
NGC 3081	37244	149.8731005	-22.82631476	PC	4/14/19 23:09	4/15/19 07:53	1675
NGC 3089	11290	149.9028701	-28.33129443	PC	4/14/19 23:09	4/15/19 07:53	1790
NGC 3079	37245	150.4908469	55.67979744	PC	4/16/19 23:00	4/17/19 04:22	1580
NGC 3227	31280	155.8774015	19.86505766	PC	4/16/19 23:00	4/17/19 04:22	1610
NGC 3786	80684	174.9271391	31.90942732	PC	4/16/19 23:00	4/17/19 04:22	1735
NGC 4151	34455	182.6357547	39.40584860	PC	4/21/19 21:41	4/22/19 06:38	1715
NGC 4180	36654	183.2626924	7.03891255	PC	4/21/19 21:41	4/22/19 06:38	1630
NGC 4235	11308	184.2911678	7.19157597	PC	4/21/19 21:41	4/22/19 06:38	1580
NGC 4388	35464	186.4449188	12.66215153	PC	4/21/19 00:00	4/22/19 00:00	1755
NGC 4593	37587	189.9143400	-5.34417010	PC	4/21/19 00:00	4/22/19 00:00	1670
NGC 5290	11388	206.3297085	41.71241871	PC	5/7/19 00:00	5/8/19 00:00	1275
NGC 5506	37274	213.3119888	-3.20768334	PC	5/7/19 03:45	5/7/19 09:42	1440
NGC 5899	36624	228.7634964	42.04991289	PC	5/7/19 03:45	5/7/19 09:42	1665
NGC 6814	32477	295.6690092	-10.32345792	PC	5/9/19 09:45	5/9/19 18:27	1665
NGC 7314	81861	338.9424567	-26.05043820	PC	5/9/19 09:45	5/9/19 18:27	1605
NGC 7378	88600	341.9486864	-11.81658744	PC	5/9/19 09:45	5/9/19 18:27	1545
NGC 7465	11341	345.5039963	15.96477472	PC	5/9/19 09:45	5/9/19 18:27	1765
NGC 7479	37294	346.2359605	12.32295297	PC	5/9/19 09:45	5/9/19 18:27	1575

Table 5. Swift XRT Observations

law continuum. In order to constrain the intrinsic flux from the power-law component at the epoch of the XRT data, we freeze the best-fit spectral parameters corresponding to components existing at large physical scales and unlikely to exhibit significant short-term variability, such as a black-body or plasma emission component, or optically-thin scattered emission. We then fit the XRT data separately from the fit that included the BAT data, determining the 90% upper limit on the power-law normalization allowable by the XRT data. We note that when using the MYTorus model the normalization of the scattered continuum is usually held fixed to that of the intrinsic power-law continuum. Because there are likely time lags of unknown duration between the intrinsic power-law emission and the scattered continuum, it is possible that the intrinsic power-law emission at the epoch of the XRT data may be considerably stronger than the scattered continuum. Fixing the scattered continuum means that a much larger range of power-law emission is allowed by the XRT data, yielding a more conservative upper limit.

As a check to ensure we are performing a core X-ray luminosity to core radio luminosity comparison, we additionally fit the Swift BAT data alone, which removes

model assumptions and potential contamination from diffuse X-ray emission at softer energies. We fit the BAT spectra with the simplest model required to adequately fit the data ($\chi^2/\text{dof} < 2$), where dof is the degrees of freedom. For 15 out of 25 objects a simple power-law was sufficient; for 5 objects a power-law with a high-energy cutoff was required; for the remainder either a power-law or cutoff power-law with an absorption component was warranted. We do not physically interpret these models or attempt to de-convolve an intrinsic power-law continuum from the fit as the 105-month BAT catalog data are limited to only 8 spectral bins. We appended the `cflux` convolution component in front of the best-fit spectral model and fit for the total observed 14–195 keV flux after freezing the power-law normalization. We found that we were able to more robustly estimate the uncertainty of the 14–195 keV flux using Markov Chain Monte Carlo (MCMC) with the default Goodman-Weare algorithm with 10 walkers. For every object we ran chains of length 10^5 after determining the appropriate burn-in period. For NGC 4180, the MCMC chain produced a bimodality in Γ with one mode at unphysically low values < 1 . We alleviated this by setting a Gaussian prior on Γ with a mean of 2.00 and stan-

dard deviation of 0.38, taken from the distribution of Γ for all AGN in the 105-month catalog, using the `bayes` command.

Finally, as we are comparing the XRT data to data from other facilities, we include in the X-ray fluxes a systematic uncertainty floor of 10% (Burrows et al. 2005), which we add in quadrature to the formal errors.

3. RESULTS AND DISCUSSION

3.1. A Comparison of VLA and VLBA Fluxes

An immediate point of interest from our initial snapshot program was the lack of VLBA detections for a majority of our sample. As our VLBA integration time calculations were derived from the FP for AGNs, we expected detections for the entirety of our sample. The left plot of Figure 4 places our sample on the FP, in comparison to data from Merloni et al. (2003), using peak radio and X-ray luminosities calculated from VLBA and Swift XRT measurements in Tables 3 and 6, respectively, and black hole mass measurements from Table 1. Targets with VLBA detections are represented by red and blue points which use simultaneous and archival XRT observations, respectively. Green points with arrows mark radio luminosity upper limits for targets with VLBA non-detections, which we define as 3σ over the RMS in each observation. From this comparison, we find that although several radio luminous targets fall within the Merloni et al. (2003) distribution, our sample lies largely below the defined plane. As the FP was derived using VLA observations, we replace our peak radio luminosities measured from our VLBA observations with peak radio luminosities from archival VLA observations in Table 4. Using these values, as shown in the right plot of Figure 4, we find our targets are 100% detected, versus 36% with VLBA, and become well-aligned with the FP and the Merloni et al. (2003) data distribution.

Our findings are consistent with those of Panessa & Giroletti (2013), who studied a more nearby ($D_L < 22$ Mpc) sample of Seyfert galaxies with the European VLBI Network (EVN), which has a similar maximum baseline to the VLBA (~ 9000 km). They find that out of 21 Seyfert galaxies observed with the EVN, 13 (62%) are detected at 5 GHz. The 90% confidence interval from binomial statistics for this fraction is 42%–79%, whereas for our targets, of which 36% were detected, the 90% confidence interval is 20%–54%, with a p-value between our study and Panessa & Giroletti (2013) of $p = 0.16$. Nonetheless, there are differences between these samples that are worth noting. First, the Panessa & Giroletti (2013) sample is again considerably closer,

with a mean distance of 14.7 Mpc,⁷ compared to the mean distance of 30.0 Mpc for our sample. Given the 3σ luminosity upper limits listed in their Table 1, the mean RMS of their EVN data is $\sim 57 \mu\text{Jy}$, about half as sensitive as our VLBA observations. The difference in mean distance and sensitivity implies that the 5 GHz observations used by Panessa & Giroletti (2013) are comparable in terms of probing the target luminosities, with upper luminosity limits about ~ 0.6 times that of our observations. Of the 20 objects in Panessa & Giroletti (2013) with 2–10 keV X-ray luminosity measurements, the mean X-ray luminosity is $8.1 \times 10^{41} \text{ erg s}^{-1}$, while for our sample the mean luminosity is $1.7 \times 10^{43} \text{ erg s}^{-1}$, indicating that higher X-ray luminosity is not necessarily correlated with greater prevalence of radio core detection at mas scales, given the statistical consistency of the latter between our study and that of Panessa & Giroletti (2013). As in this work, Panessa & Giroletti (2013) also find that the X-ray emission is more correlated with larger-scale radio emission as captured by the archival VLA observations they use, and they suggest that this implies that the hard 2–10 keV luminosity in an AGN is associated with larger-scale structure than the radio core. With both 5 GHz and 1.7 GHz VLBI observations, they are able to estimate spectral index α , and find that the disparity between the VLA and VLBI fluxes is less in flatter-spectrum objects, consistent with the emission being truly core-dominated.

It is interesting to note that other studies aimed at detecting radio quiet quasars on spatial scales of the VLBA using ancillary catalogs such as those from the VLA as a priori source lists find similar detection rates to the ones we find in this work. For example, the recent work by Herrera Ruiz et al. (2017) mosaic the COSMOS field with the VLBA at 1.4 GHz and find a detection rate of $\sim 20\%$ for all VLA detected sources at 3 GHz. Herrera Ruiz et al. (2018) followed up this work by combining the Robert C. Byrd Green Bank Telescope together with the VLBA (VLBA+GBT) for increased sensitivity at 1.4 GHz and detected an additional 10 sources that were not previously seen with the VLBA alone. The overall detection rate for this follow-up study, however, remained at $\sim 20\%$. Similarly, Middelberg et al. (2013) mosaicked the Lockman Hole/XMM field with the VLBA at 1.4 GHz and out of their parent sample of 217 sources, only 65 sources ($\sim 30\%$) were, in fact, detected at their 1σ sensitivity threshold of $\sim 20 \mu\text{Jy beam}^{-1}$. Although these studies present results at a different frequency than

⁷ Panessa & Giroletti (2013) also use a flat Λ CDM with $H_0 = 70 \text{ km s}^{-1} \text{ Mpc}^{-1}$ and $\Omega_M = 0.3$.

our study (1.4 GHz versus 6 GHz), the radio emission across both of these frequencies is expected to be dominated by synchrotron, non-thermal emission processes (see e.g., Condon 1992, for a discussion on radio emission in galaxies). There are clear differences in the observing strategies, sensitivity limits, and populations of radio quasars studied by Panessa & Giroletti (2013), Herrera Ruiz et al. (2017, 2018), Middelberg et al. (2013) and our volume-complete sample, but the detection rates from all of these studies are within the $\sim 20\text{-}40\%$ range, which may be pointing to a similar process responsible for the core radio emission seen in AGNs at these VLBA spatial scales.

To explore this idea further, we compare the VLBA and VLA peak and integrated flux density measurements in our targets. We find the difference in peak flux measurements between VLBA and VLA observations appear to be greater in targets such as NGC 1068 and NGC 2992, with VLBA measurements that place them further from the Fundamental Plane as shown in Figure 5. We also find that targets further from the Fundamental Plane have more extended 6 cm radio morphologies in our VLA observations. We quantify this by measuring the ratio between the VLA flux peak (F_{peak}) and the VLA integrated flux density greater than $5\times$ RMS (F_{int}) using values listed in Table 4, where more extended targets have a greater portion of their flux outside the nucleus and a ratio closer to zero. Further, we find a relationship between these two ratios, where AGN with greater VLA/VLBA flux ratios are typically more extended as they exhibit larger VLA F_{peak}/F_{int} ratios. Together, these relationships suggest that the emission observed in VLA observations is largely extended, where AGN that deviate further from the Fundamental Plane have larger differences in VLA and VLBA peak flux measurements and exhibit more extended radio emission relative to the nucleus. Additionally, we can show that emission measured in VLA observations is extended in targets with VLBA non-detections by comparing our VLA peak-flux measurements to the VLBA background RMS as listed in Table 3. Assuming that the VLA emission originated from a point source, one would expect to detect said source in the VLBA observations with a signal-to-noise $S/N = F_{peak}(VLA)/VLBA_{RMS}$. We measure this hypothetical S/N ratio to be > 3 in all targets with VLA observations, with $S/N > 5$ in 10 of 11 targets, suggesting a point source would have been detected for each AGN if present.

Following Zakamska & Greene (2014), we suggest that the extended radio emission observed in the VLA observations for this sample is largely a by-product of relativistic particles accelerated in shocks caused by AGN-

driven winds, similar to processes in supernova remnants. Assuming a scenario where radio emission in each of these targets is attributed to a jet emanating from the nucleus, one would expect larger discrepancies between VLA and VLBA observations in compact sources, where the jet is pointed along our line of sight. Instead of being spread across the plane of the sky, the bulk of the extended, contaminating emission in these targets would be contained near the nucleus along our line of sight, captured in VLA observations but resolved out in VLBA observations. As we note, we find larger ratios to exist between VLA and VLBA peak flux measurements in targets with more extended morphologies, thus it is likely that we are not observing an effect dependent on the orientation of the AGN with respect to our line of sight. Instead, in a scenario where emission is formed by shocks via AGN feedback, the observed ratio between VLA and VLBA fluxes would be dependent on the orientation of the AGN with respect to its host galaxy, where targets in our sample with extended VLA morphologies are exhibiting more interactions between the AGN and its host medium than targets with compact VLA morphologies.

These interactions translate down to parsec-scale levels, where VLA peak-flux measurements of our AGN are likely contaminated by unresolved extra-nuclear host interactions that resolve out of VLBA peak-flux observations with the AGN becoming much less luminous than hypothesized from the Fundamental Plane relation. We see this explicitly in VLBA observations of NGC 1068 in Figure 6 which exhibit several knots of extra-nuclear emission in addition to the AGN, whose position was previously identified by Gallimore et al. (2004) and references therein. Placing the synthesized beam and flux peak location obtained from the archival VLA observations onto our VLBA observations, we see that the peak flux measured by the VLA is derived largely from extra-nuclear emission north of the nucleus and likely does not contain emission from the AGN itself. While the source at the center of the VLA beam and the central AGN exhibit similar peak fluxes in our VLBA measurements, MERLIN observations from Gallimore et al. (2004) reveal the non-AGN source to be much more luminous at scales slightly larger (MERLIN restoring beam ~ 60 mas) than what is resolvable by VLBA (maximum resolvable size ~ 47 mas). We note that NGC 1068 is the only source in our sample that exhibits such a misalignment between VLA peak and VLBA peak, which likely accounts for the extreme ratio between VLA and VLBA fluxes for NGC 1068 compared to the seven other sources shown in Figure 5. However, even without a misalignment where the VLA peak flux would have been cen-

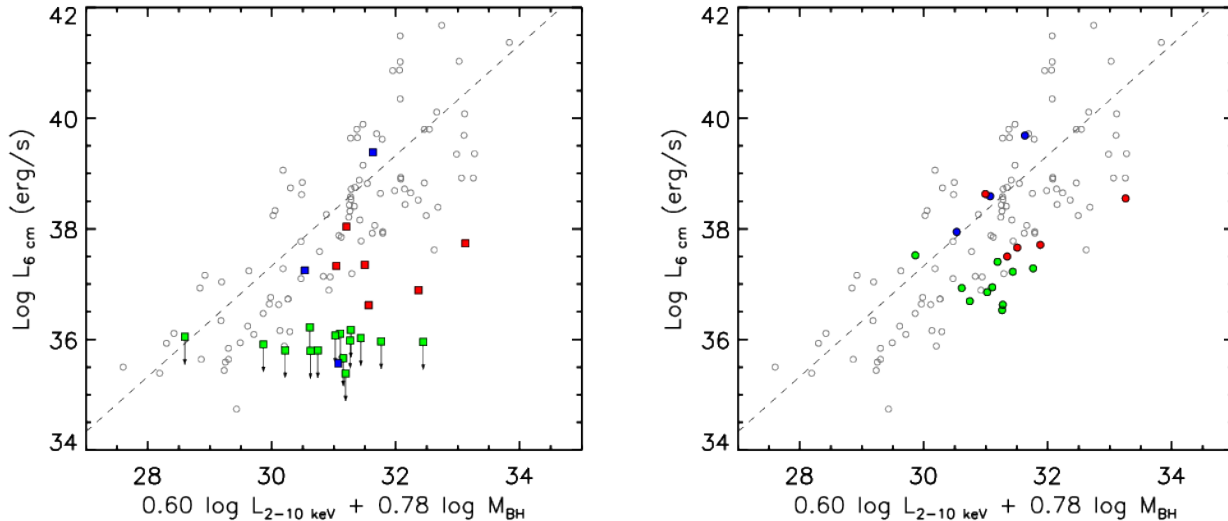


Figure 4. Distribution of our sample on the FP described by Merloni et al. (2003) using peak radio luminosities derived from *left*: VLBA observations and *right*: VLA observations (when available). Red points represent targets with simultaneous VLBA and Swift XRT observations. Blue points represent targets with new VLBA observations and archival Swift XRT observations. Green points are targets with VLBA observations where we estimate the upper limit of L_R in the targets as $5 \times \text{RMS}$. Grey circles and dashed line represent measurements and best fit from Merloni et al. (2003).

tered over the AGN, Figure 6 also exhibits several knots of extra-nuclear emission adjacent to the central engine which would contaminate VLA peak-flux measurements for NGC 1068.

3.2. The Fundamental Plane at High Physical Resolution

We have shown that, when probed at the exquisite angular resolution of the VLBA, AGN are under-luminous or altogether undetected, at odds with their properties in lower angular resolution VLA data, but potentially more in line with the scaling relation for Galactic X-ray binaries. We can remove the dependence of black hole mass in this relation for a pure comparison between X-ray and radio luminosities and produce a relationship that may better encapsulate the core behavior of AGNs. Figure 7 compares $L_{6 \text{ cm}}$ and $L_{2-10 \text{ keV}}$ in our sample, with detections as red points and radio luminosity upper-limits derived from RMS values for non-detections as green points, revealing VLBA observed AGN largely fall in line with measurements for Galactic black holes (GBHs). While the majority of our sample is undetected, these non-detections are significant and so in order to preserve the statistical power of our sample we fold in the information these non-detections carry by performing regression with censored data using the ASURV package (Lavalley et al. 1992).

$L_5 \text{ GHz}$ and $L_{2-10 \text{ keV}}$ measurements from Table 1 of (Panessa & Giroletti 2013) are also included as blue points. Initially, there appears to be a discrepancy be-

tween how both datasets compare to measurements from GBHs. However, separating radio-quiet and radio-loud AGN according to the X-ray radio loudness parameter ($R_X \equiv L_{6 \text{ cm}}/L_{2-10 \text{ keV}}$ limit ($R_X = -4.5$) from Terashima & Wilson (2003), we find the eight radio-loud AGN in the Panessa & Giroletti (2013) sample are the targets which do not strongly agree with the general trend. Additionally, NGC 1052 from our sample is also radio-loud by this definition, likewise separating itself from the general trend, which concurs with its use as an ICRF target and the documented presence of a relativistic radio jet (Lister et al. 2019) often present in radio-loud AGN. We note that while GBHs may themselves exhibit bimodality in L_R/L_X (e.g., Gallo et al. 2012), these modes do not appear to be reflected in the AGN population. Using the two best-fit relations from Gallo et al. (2012), the GBHs in this work are consistent with one or the other, but both relations predict radio luminosities that are three to four orders of magnitude below the radio-loud relation at the X-ray luminosities of AGNs. Of the two GBH L_R/L_X “tracks” presented in Gallo et al. (2012), the lower track, corresponding to GBHs that are less radio-luminous, is more consistent with the AGNs studied in this work.

As even completely uncorrelated fluxes can become highly correlated when multiplied by random distances spanning several orders of magnitude, we fit the FP in terms of flux as well as luminosity normalized by BH mass. The results are shown in Figure 8, which show that the correlation between the 2–10 keV and 6 cm

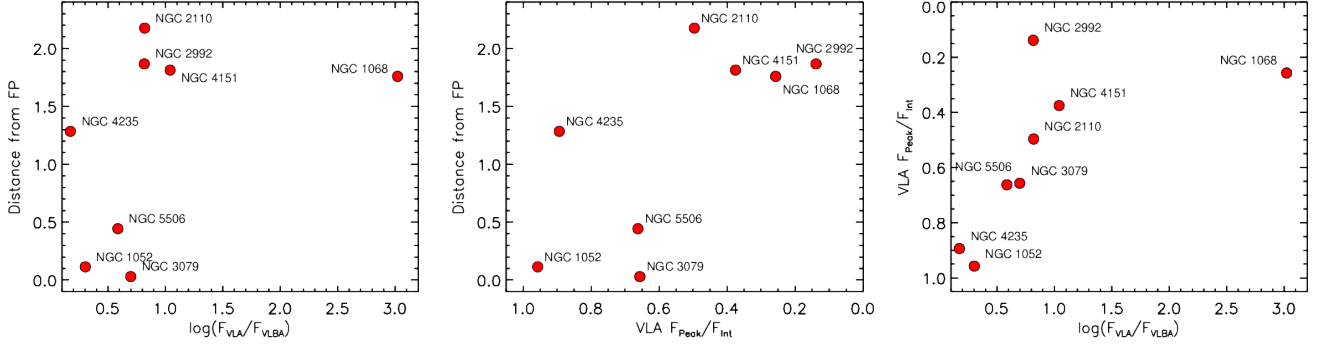


Figure 5. Comparisons between ratio of integrated to peak VLA flux, ratio of peak VLA to peak VLBA flux, and distance from the Fundamental Plane in dex.

Object	Model	Total stat/dof	N_{H} cm^{-2}	Γ	$\log_{10}(F_{2-10 \text{ keV}})$ [$\text{erg cm}^{-2} \text{ s}^{-1}$]
NGC 2110	phabs*pow + const*pow	383.25/473	$6.8^{+2.1}_{-1.7} \times 10^{22}$	$2.5^{+0.6}_{-0.5}$	$-10.12^{+0.05}_{-0.04}$
NGC 2782	apec + zpow + const*pow	29.31/30	$1.4^{+0.3}_{-0.1} \times 10^{23}$	$1.8^{+0.5}_{-0.5}$	$-11.9^{+0.5}_{-0.4}$
NGC 2992	phabs*pow	358.22/416	$7.5^{+1.9}_{-1.7} \times 10^{21}$	$1.6^{+0.2}_{-0.2}$	$-10.00^{+0.02}_{-0.02}$
NGC 3079	vapc + MYTorus	120.30/95	$8.5^{+1.2}_{-1.0} \times 10^{24}$	$2.2^{+0.1}_{-0.1}$	-9.9
NGC 3081	apec + MYTorus	41.05/34	$6.1^{+0.4}_{-0.3} \times 10^{23}$	$1.96^{+0.01}_{-0.01}$	$-10.5^{+0.1}_{-0.2}$
NGC 3089	phabs*pow	28.55/27	$7.1^{+5.4}_{-3.5} \times 10^{22}$	$2.7^{+1.1}_{-0.8}$	$-11.7^{+0.2}_{-0.1}$
NGC 3227	pow	290.09/292	$< 6.1 \times 10^{20}$	$1.7^{+0.1}_{-0.1}$	$-10.10^{+0.03}_{-0.03}$
NGC 4151	zbody + zxicf*zcutoffpl	258.15/328	$7.8^{+2.2}_{-2.0} \times 10^{22}$	$1.51^{+0.03}_{-0.03}$	$-9.60^{+0.06}_{-0.08}$
NGC 4180	MYTorus	5.40/2	$7.3^{+1.7}_{-1.5} \times 10^{24}$	$1.5^{+0.3}_{-0.2}$	-11.1
NGC 4235	phabs*pow	150.28/181	$2.7^{+1.6}_{-1.4} \times 10^{21}$	$1.7^{+0.3}_{-0.3}$	$-11.13^{+0.06}_{-0.06}$
NGC 4388	phabs*pow + const*pow	248.06/265	$4.6^{+1.0}_{-0.9} \times 10^{23}$	$3.2^{+1.0}_{-0.9}$	$-9.5^{+0.2}_{-0.1}$
NGC 4593	pow	304.40/353	$< 2.7 \times 10^{20}$	$1.6^{+0.09}_{-0.09}$	$-10.45^{+0.03}_{-0.03}$
NGC 5290	phabs*pow	114.27/145	$9.5^{+6.5}_{-5.3} \times 10^{21}$	$1.1^{+0.5}_{-0.5}$	$-10.83^{+0.05}_{-0.05}$
NGC 5506	zxicf*pexrav	257.79/304	$1.2^{+0.6}_{-0.1} \times 10^{22}$	$1.7^{+0.3}_{-0.2}$	$-9.97^{+0.10}_{-0.03}$
NGC 5899	phabs*pow	51.39/49	$10.9^{+5.1}_{-3.8} \times 10^{22}$	$2.0^{+0.2}_{-0.2}$	$-11.1^{+0.1}_{-0.1}$
NGC 6814	pow	324.07/350	$< 5.4 \times 10^{20}$	$1.6^{+0.1}_{-0.1}$	$-10.68^{+0.03}_{-0.03}$
NGC 7314	phabs*pow	247.97/293	$8.6^{+1.4}_{-1.3} \times 10^{21}$	$1.9^{+0.1}_{-0.1}$	$-10.69^{+0.03}_{-0.03}$
NGC 7378	phabs*pow	8.94/9	$5.8^{+2.2}_{-2.1} \times 10^{22}$	$1.7^{+0.1}_{-0.1}$	$-12.1^{+1.1}_{-0.2}$
NGC 7465	phabs*pow	166.46/215	$8.2^{+3.0}_{-2.6} \times 10^{21}$	$1.6^{+0.3}_{-0.2}$	$-10.95^{+0.05}_{-0.05}$
NGC 7479	apec + MYTorus	15.52/9	$5.7^{+0.5}_{-0.5} \times 10^{24}$	$2.5^{+0.1}_{-0.1}$	-8.8

Table 6. X-ray spectral fitting results. All (formal) confidence intervals and upper limits are 90% except for the X-ray fluxes, which are $\pm 1\sigma$. X-ray fluxes without a confidence interval are from fits not using contemporaneous Swift XRT data. Note that Swift XRT was in an anomaly state for NGC 3786, so we could not use its data.

fluxes and BH mass-normalized luminosities is weak, and that the values derived using the high physical resolution VLBA data overlap with the values seen in XRBs, which are systematically lower than AGNs observed in lower-resolution studies.

Finally, we compared the radio luminosities to the observed 14–195 keV luminosities from the 105-month BAT spectra alone, using the fluxes calculated in Section 2.6 and provided in Table 7. For the X-ray data

from the Merloni et al. (2003) sample, which was mostly taken from published literature using a wide variety of X-ray observatories, we multiply the 2–10 keV luminosities by a factor of 1.6 to estimate the 14–195 keV luminosities, a factor derived from a power-law with a spectral index of 2. The results are shown in the right panel of Figure 7. As can be seen, the 2–10 keV fluxes calculated using our simultaneous Swift XRT observations are consistent with those inferred from the BAT

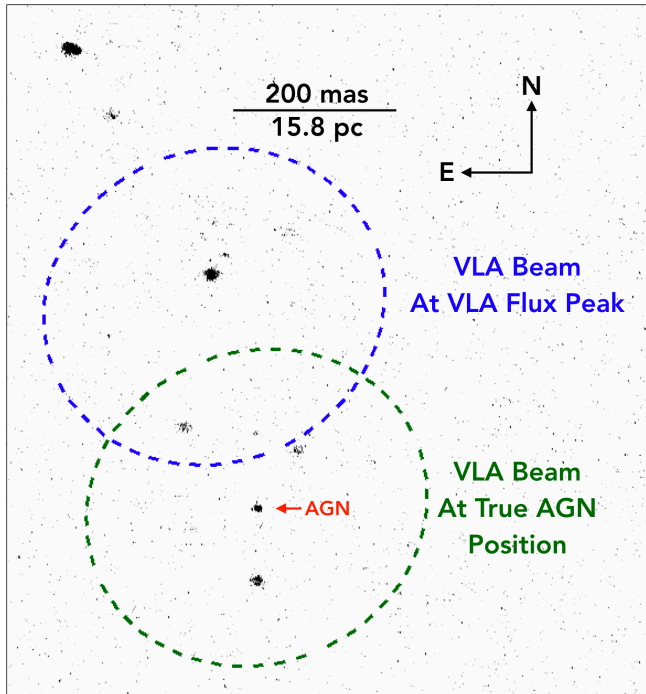


Figure 6. Extended 5 GHz VLBA imaging of NGC 1068 showing the central AGN, and adjacent, extra-nuclear emission. Larger, dashed ellipses represent the synthesized beam size of the corresponding 5 GHz VLA observation. The northern, blue ellipse is centered on the VLA flux peak, and the southern, green ellipse is centered on the AGN. Both ellipses illustrate that extra-nuclear radio emission can contaminate VLA peak flux measurements. The red arrow points to the nuclear AGN emission shown in Figure 2.

data, indicating that apparent under-luminosity seen in the radio between VLA and VLBA data is not in fact due to an over-luminosity at softer X-rays due to contamination from extra-nuclear sources.

3.3. The Nature of Sub-Parsec-Scale Radio Emission

With the results detailed in Section 3.1 and Section 3.2, it is clear that there is a resolution dependence of the perceived radio luminosity of nearby AGNs, that at sub-parsec scales the radio emission is considerably less luminous, and that the FP does not appear to capture the relationship between the black hole mass, X-ray luminosity, and radio emission at these scales. It is therefore worthwhile to explore what physical mechanisms may be behind the radio emission that we do detect on mas scales.

In higher-frequency studies (e.g., 22 GHz Baek et al. 2019; Smith et al. 2020), there may be some mixture of synchrotron and thermal bremsstrahlung (free-free) emission, which begins to dominate for star-forming galaxies above ~ 30 GHz (Condon 1992). However, for our observations, which were taken at 5 GHz, it is more

Object	Model	χ^2/dof	$\log_{10} (F_{14-195 \text{ keV}})$ [erg cm $^{-2}$ s $^{-1}$]
NGC 1052	pow	4.87/5	$-10.505^{+0.036}_{-0.046}$
NGC 1068	phabs*pow	2.51/4	$-10.515^{+0.031}_{-0.047}$
NGC 1320	pow	3.31/5	$-10.872^{+0.067}_{-0.121}$
NGC 2110	cutoffpl	4.16/4	$-9.496^{+0.004}_{-0.006}$
NGC 2782	pow	1.45/5	$-10.921^{+0.068}_{-0.136}$
IC 2461	pow	3.26/5	$-10.722^{+0.011}_{-0.025}$
NGC 2992	pow	1.43/5	$-10.487^{+0.035}_{-0.046}$
NGC 3079	phabs*cutoffpl	2.78/3	$-10.550^{+0.053}_{-0.008}$
NGC 3081	phabs*cutoffpl	1.53/3	$-10.125^{+0.012}_{-0.026}$
NGC 3089	pow	0.76/5	$-11.156^{+0.072}_{-0.248}$
NGC 3227	phabs*cutoffpl	4.34/3	$-9.990^{+0.015}_{-0.010}$
NGC 3786	pow	2.1/5	$-10.836^{+0.058}_{-0.095}$
NGC 4151	cutoffpl	7.11/4	$-9.249^{+0.003}_{-0.002}$
NGC 4180	pow	9.14/5	$-10.847^{+0.074}_{-0.139}$
NGC 4235	pow	4.29/5	$-10.414^{+0.028}_{-0.034}$
NGC 4388	pow	2.18/4	$-9.569^{+0.005}_{-0.005}$
NGC 4593	cutoffpl	0.87/4	$-10.112^{+0.034}_{-0.013}$
NGC 5290	pow	2.54/5	$-10.835^{+0.054}_{-0.076}$
NGC 5506	phabs*cutoffpl	2.93/3	$-9.700^{+0.013}_{-0.004}$
NGC 5899	pow	2.03/5	$-10.688^{+0.037}_{-0.053}$
NGC 6814	cutoffpl	2.18/4	$-10.258^{+0.050}_{-0.012}$
NGC 7314	cutoffpl	0.44/4	$-10.335^{+0.046}_{-0.018}$
NGC 7378	pow	2.21/5	$-10.863^{+0.079}_{-0.170}$
NGC 7465	pow	3.5/5	$-10.722^{+0.055}_{-0.083}$
NGC 7479	pow	5.31/5	$-10.774^{+0.058}_{-0.096}$

Table 7. Best-fit XSPEC models for the Swift BAT data from the 105-month catalog (Oh et al. 2018), with observed 14–195 keV fluxes.

likely that the emission is synchrotron-dominated. This is not necessarily true, however, if the radio emission is “young”, which induces a spectral curvature, or turnover at lower frequencies. One means of distinguishing these emission mechanisms is by calculating the brightness temperature:

$$T_b = \frac{4 \ln(2) c^2 S_\nu}{2\pi k_B \theta_A \theta_B}, \quad (1)$$

where S_ν is the specific intensity over the solid angle, and θ_A and θ_B are the full widths at half power of the major and minor axes of an elliptical Gaussian beam. We find that the brightness temperatures calculated from our VLBA detections range from $10^{6.1}$ K to $10^{9.7}$ K, indicating a likely dominant synchrotron source. One potential source of compact emission, thermal free-free emission from accretion disk winds, may be significantly present in NGC 1068 and NGC 2992, which

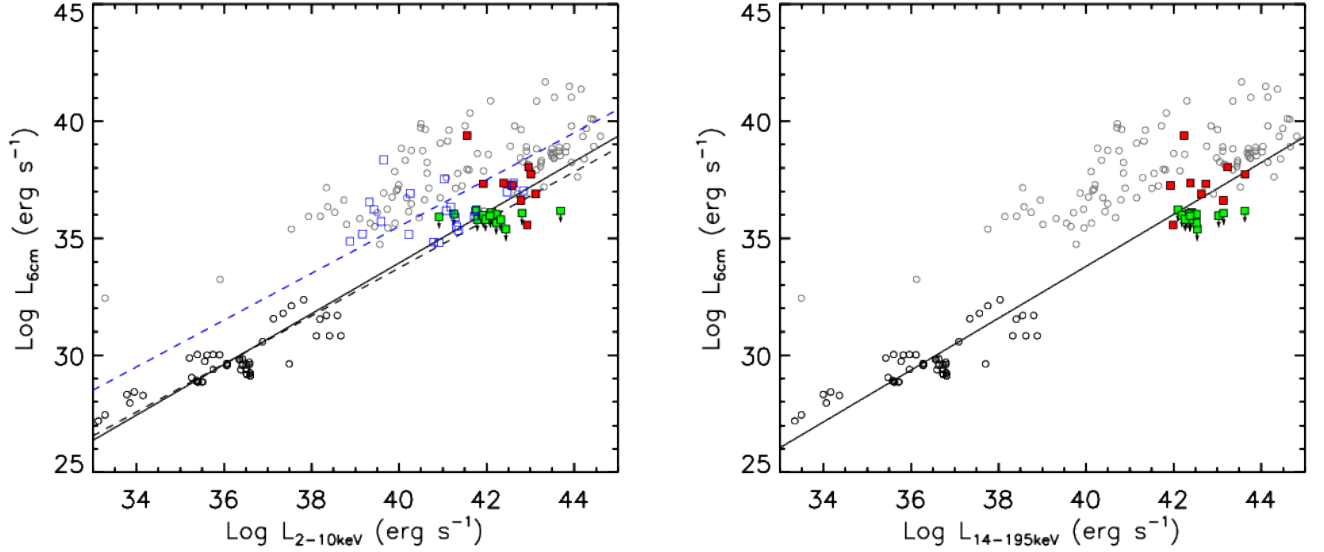


Figure 7. Comparison between radio and X-ray luminosities in our sample, Panessa & Giroletti (2013), and Merloni et al. (2003) for Galactic and extragalactic black holes. *Left:* Red and green squares designate measurements for our detected sources and upper limits on undetected sources, respectively. Open blue squares designate measurements from Panessa & Giroletti (2013). Open grey and black circles represent SMBH and GBH measurements from Merloni et al. (2003), respectively. Solid line represents the best fit between our detected sources and GBHs from Merloni et al. The black dashed line represents the best fit also including the upper limits from our non-detections. The blue dashed line represents the X-ray radio loudness parameter of $R_X \equiv L_R/L_X = -4.5$. *Right:* Similar comparison using 14-195 keV measurements of our sample compared to 2-10 keV luminosities from Merloni et al. scaled by 1.6.

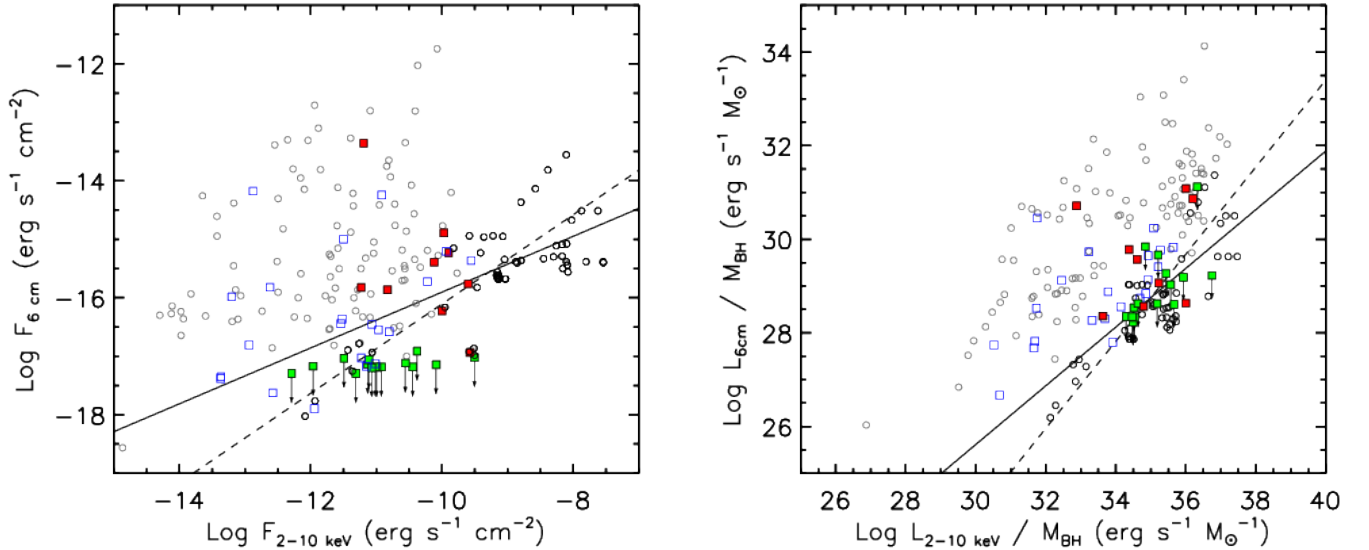


Figure 8. Comparison between radio and X-ray flux measurements (*left*) and radio and X-ray luminosities divided by black hole mass (*right*) in our sample and Merloni et al. (2003) for Galactic and extragalactic black holes. Red and green squares designate measurements for our detected sources and upper limits on undetected sources, respectively. Open blue squares designate measurements from Panessa & Giroletti (2013). Open grey and black circles represent SMBH and GBH measurements from Merloni et al. (2003), respectively. Solid line represents the best fit between our detected sources and GBHs from Merloni et al. Dashed line represents the best fit also including the upper limits from our non-detections.

have brightness temperatures of $10^{6.1}$ K and $10^{6.3}$ K, respectively. NGC 1068 exhibits extreme line-of-sight absorption $N_{\text{H}} \sim 10^{25} \text{ cm}^{-2}$ (Ricci et al. 2017), which may scatter or absorb direct non-thermal AGN emission (Gallimore et al. 1997, 2004). For the remaining objects, $T_b \geq 10^7$, suggesting either jet-associated or corona-associated synchrotron. While our observations sample down to the parsec or sub-parsec scale, it is possible that sub-parsec jets may exist, as was recently found for a small fraction (4%) of BAT-selected AGNs using other VLBI observations (Baek et al. 2019). However, the AGNs in that study are more distant, with radio luminosities several orders of magnitude larger than the sample studied here. Indeed, Baek et al. (2019) find that the L_R/L_X relation of their sample spans a range of $10^{-3.5} - 10^{-1.5}$, indicating jet-dominated radio emission. By contrast, our sample has L_R/L_X between $\sim 10^{-7} - 10^{-4}$, more in line with expectations from coronal emission, which scales as approximately $L_R/L_X \sim 10^{-5}$ (Laor & Behar 2008; Panessa et al. 2019).

If the radio emission is coronal in origin, then one might expect that the relationship between the X-ray luminosity, radio luminosity, and black hole mass would be more pronounced (i.e., a tighter FP), on account not only of the X-ray and radio emission originating in the same physical structure, but also that structure existing only a few gravitational radii from the black hole (e.g., Reis & Miller 2013). However, we have found that the correlation between the X-ray and parsec-scale radio emission in hard X-ray selected AGNs is rather poor, and is not improved by the introduction of the black hole mass. Indeed, the majority of our sample is not even detected in the radio on parsec scales, in stark contrast with lower resolution studies (e.g., Smith et al. 2020), with L_R/L_X well below the fiducial 10^{-5} scaling for pure coronal emission (Laor & Behar 2008; Panessa et al. 2019). We suggest that there may be “radio silent” AGNs: AGNs that do not even produce significant coronal synchrotron radio emission. Deeper follow-up studies of these undetected sources will prove critical to confirming this, but in either case our results underscore the need to better understand and characterize the physical properties of the corona.

4. CONCLUSIONS

In this work, we have explored the simultaneous X-ray (2–10 keV) and radio (C-band; 5 GHz) properties of a complete sample of AGNs with hard X-ray (14–195 keV) luminosities above $10^{42} \text{ erg s}^{-1}$ from the local volume out to 40 Mpc, within the declination limits of -30° to $+60^\circ$. Our X-ray observations, which

come from Swift XRT, have allowed us to fit the X-ray spectra of our targets, factoring in prior information from the long-term average BAT spectra, obtaining absorption-corrected 2–10 keV luminosities for comparison with the radio to X-ray luminosity relation L_R/L_X , as well as the Fundamental Plane of black hole activity, the latter of which seeks to unify the radio and X-ray accretion properties of both Galactic and supermassive black holes by including the black hole mass as a third parameter. Our radio observations, which come from the VLBA, were designed to achieve good uv coverage, and have allowed us to probe the radio emission of these AGNs in the sub-parsec regime, at the cost of sensitivity to large-scale extended radio emission. These data have therefore enabled a systematic study of the contemporaneous relationship between the X-ray corona and the origin of core radio emission in AGNs, a relationship that is not currently well understood. Our conclusions are as follows:

1. AGN fall out of the Fundamental Plane when radio fluxes are measured on mas (sub-parsec) scales. The difference in flux between VLBA and VLA observations suggests that measurements made with the VLA are contaminated by additional extranuclear radio emission that is resolved out in VLBA observations, and that this extended extranuclear radio emission is responsible for the Fundamental Plane.
2. Radio-quiet AGN share a similar relationship between $L_{5 \text{ GHz}}$ and $L_{2-10 \text{ keV}}$ with nearby Galactic black holes. Radio-loud AGN ($R_X < -4.5$) do not share this relation and do not appear to have Galactic black hole analogs.
3. These results are consistent with a fundamental bimodality in L_R/L_X for AGNs, supporting their classification as either radio-loud or radio-quiet. Caution is therefore warranted when extrapolating physical models of nearby AGNs to their higher redshift, radio-bright counterparts.
4. Despite the depth of our VLBA observations (RMS $\sim 20 \mu\text{Jy}$), the majority of our sample is undetected, with hard upper limits (3σ) on the L_R/L_X relation as low as $< 10^{-7}$, below even expectations from their coronal X-ray emission, which scales as approximately $L_R/L_X \sim 10^{-5}$, suggesting AGNs that are effectively “radio-silent”. These findings underscore the need for further dedicated study of the physics of the X-ray corona.

ACKNOWLEDGMENTS

We thank Claudio Ricci for helpful suggestions regarding the X-ray analysis.

The National Radio Astronomy Observatory is a facility of the National Science Foundation operated under cooperative agreement by Associated Universities, Inc. The authors acknowledge use of the Very Long Baseline Array under the US Naval Observatory’s time allocation. This work supports USNO’s ongoing research into

the celestial reference frame and geodesy. This work made use of data supplied by the UK Swift Science Data Centre at the University of Leicester. The images used throughout this work were made using APLpy. (Robitaille & Bressert 2012).

Facilities: VLBA, Swift, VLA, EVLA

Software: AIPS, Astropy (Astropy Collaboration et al. 2013), CASA, XSPEC

APPENDIX

A. NOTES ON INDIVIDUAL OBJECTS

NGC 2782

This object was suggested to be Compton-thick by Zhang et al. (2006), who fit Chandra X-ray Observatory (CXO) data with a plasma emission component plus a high-energy reflection model. Tzanavaris & Georgantopoulos (2007), using the same data, notice an Fe $K\alpha$ line (6.4 keV) at high significance with an equivalent width (EW) of ~ 1.5 keV. We use an APEC model to account for the plasma component, setting the temperature and abundance equal to the values in Zhang et al. (2006), and fit the spectrum using MYTorus. We obtain a column density N_{H} value of $1.3^{+4.7}_{-1.3} \times 10^{23} \text{ cm}^{-2}$, suggesting that the source is heavily absorbed if not Compton-thick. However, the relative normalization between the scattered (“reflection”) continuum and the intrinsic power-law component is over four orders of magnitude different between time-averaged BAT spectrum and the XRT data, despite their intrinsic power-law fits varying in normalization only marginally, which is unphysical. Conversely, if we assume that the relative normalization of the scattered continuum is constant between epochs, the best-fit N_{H} is unchanged but the intrinsic power-law normalization corresponding to the XRT data is $\sim 25\%$ that of the BAT data, indicating considerable variability. Setting the strength of the scattered continuum to be fixed between the BAT and XRT epochs, which allows for the possibility of a time delay between a change in the intrinsic power-law continuum and a change in the scattered continuum, leaves this result unchanged, likely due to the weakness of the scattered continuum at low N_{H} values. However, the complex nature of the soft X-ray spectrum allows for a wide range of possible N_{H} values, as we have seen. To mitigate this issue, we downloaded and reprocessed the archival CXO data discussed above (Obs ID 3014; 2002 May 17; PI: Stevens) using CIAO, version 4.10 with CALDB 4.7.8. Using a $r = 1''.5$ aperture centered on the AGN, and defining an $1''.4 < r < 3''.5$ annular background region immediately surrounding the AGN to sample the diffuse soft X-ray emission that contaminates the low angular resolution XRT data (Figure 9), we extracted the isolated AGN spectrum using `specextract`. With the AGN isolated, we were able to delete the diffuse plasma APEC component, fitting only the MYTorus model. We find a hydrogen column density of $N_{\text{H}} = 1.4^{+0.3}_{-0.1} \times 10^{23} \text{ cm}^{-2}$, consistent with the best-fit value using the XRT data, but with significantly tighter confidence bounds. We therefore classify NGC 2782 as not being Compton-thick, contrary to the findings of Zhang et al. (2006). With N_{H} frozen to this value, we re-fit the XRT+BAT data, finding that the power-law normalization at the XRT epoch is 26% that of the BAT data, in agreement with our initial finding of variability between the epochs. Finally, we note that, in addition to diffuse soft X-ray emission, there are 5 unresolved X-ray sources within the XRT aperture, consistent with being X-ray binaries (XRBs) or background AGNs (Figure 9). We extracted the background-isolated summed spectrum for all 5, finding it to be well-fit ($\chi^2/\text{dof} = 1.03$) with a power-law component with $\Gamma = 1.7$ and $N_{\text{H}} = 6.5 \times 10^{20} \text{ cm}^{-2}$. The total 2–10 keV flux is $3.5 \times 10^{-14} \text{ erg cm}^{-2} \text{ s}^{-1}$, $\sim 3\%$ of the flux from the absorbed power-law component fit to the XRT data. We therefore do not consider these sources to be a significant contaminant in our results.

NGC 3079

This is a known Compton-thick object (e.g., Ricci et al. 2017), and has an extensive nuclear superbubble (e.g., Li et al. 2019) that contributes significantly to the X-ray spectrum at soft (< 2 keV) energies. As with NGC 2782, we isolate the nuclear X-ray emission using CXO data (Obs ID 19307; 2018 January 30; PI: Li), using the immediate vicinity of the AGN for the background spectrum. We also found an archival NuSTAR observation (Obs ID 60061097002;

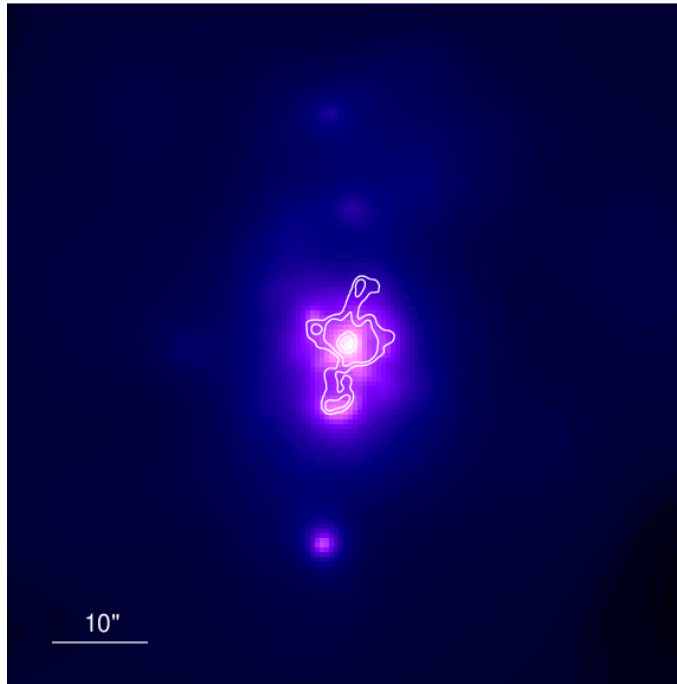


Figure 9. NGC 2782 CXO 0.5–10 keV image (adaptively smoothed). For reference we also include C-band (6 GHz) contours from an archival B/A-configuration VLA observation, showing how the extended X-ray emission coincides with the extended radio continuum. Image is approximately the same size as the XRT extraction aperture.

2013 November 12; PI: Harrison) taken as part of the NuSTAR extragalactic surveys (Harrison et al. 2016). Using MYTorus, we found a good fit ($\chi^2/\text{dof} = 197.95/155$) with $N_{\text{H}} = 8.5_{-1.0}^{+1.2} \times 10^{24} \text{ cm}^{-2}$, although we have to fit the CXO and NuSTAR data respectively above 4 and 7 keV to avoid residual contamination from the diffuse X-ray emission seen in the CXO image (Figure 10). We show this spectrum in Figure 11. We note that we find evidence of variability in the intrinsic power-law spectral index Γ between the NuSTAR and BAT data, with the former having $\Gamma = 1.7_{-0.2}^{+0.2}$ and the latter having $\Gamma = 2.2_{-0.1}^{+0.1}$.

We then fit the XRT and BAT data separately, holding the MYTorus component parameters fixed to the best-fit values found above, and adding before the MYTorus component an Astrophysical Plasma Emission Code (APEC; Smith et al. 2001)⁸ model, using the default `anqr` abundances (Anders & Grevesse 1989). With the exception of the normalization, we keep all APEC parameters frozen to those found in Li et al. (2019) by using the `vapcc` variant. Although the intrinsic power-law continuum is of course not detectable in the XRT data for this bone fide Compton-thick object, precluding a measurement of the unabsorbed 2–10 keV flux contemporaneous with our VLBA observations, the XRT data do reveal the presence of additional X-ray emission above ~ 1 keV not attributable to the plasma emission component. We find that this additional emission is consistent with an optically-thin scattered continuum component, which can be interpreted as intrinsic power-law emission originating along an unobscured direction being scattered off free electrons back into our line of sight. We model this component as a power-law with parameters held fixed to the intrinsic power-law component fit to the BAT data, with a coefficient to account for the scattering fraction. We find this value to be $\sim 0.1\%$. We show this spectrum in Figure 12.

NGC 3081

One archival CXO observation exists for this object (Obs ID 20622; 2018 January 24; PI: Maksym). The high angular resolution X-ray imaging enabled by these data reveal a compact source with little diffuse emission and few nearby XRBs (Figure 13). A joint analysis of the CXO and BAT spectrum gives an excellent fit ($\chi^2/\text{dof} = 141.93/141$) with an APEC thermal plasma model appended to MYTorus, consistent with the findings of Eguchi et al. (2011) who performed a joint fit with Suzaku and Swift BAT 22-month catalog data (Tueller et al. 2010). However, by allowing

⁸ <http://www.atomdb.org>

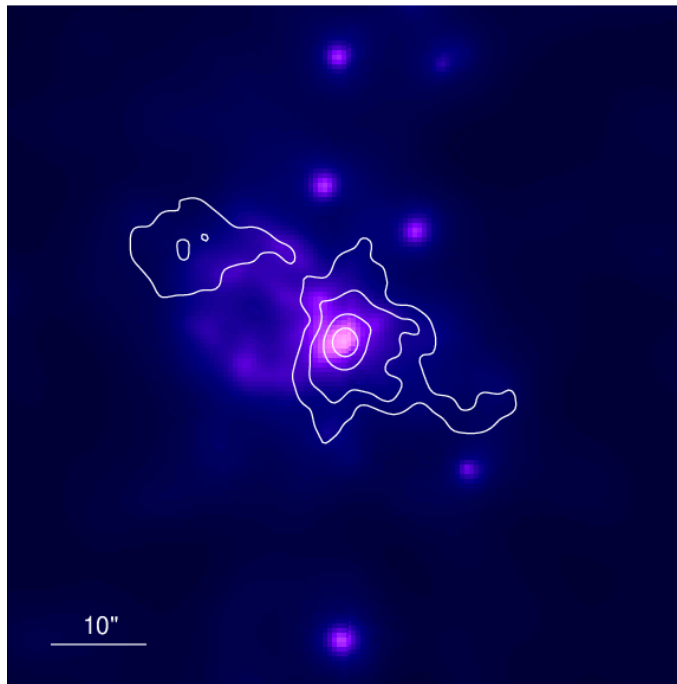


Figure 10. NGC 3079 CXO 0.5–10 keV image (adaptively smoothed). For reference we also include L-band (1.4 GHz) contours from an archival A-configuration VLA observation, showing extended radio emission ahead of the loop of soft X-ray emission.

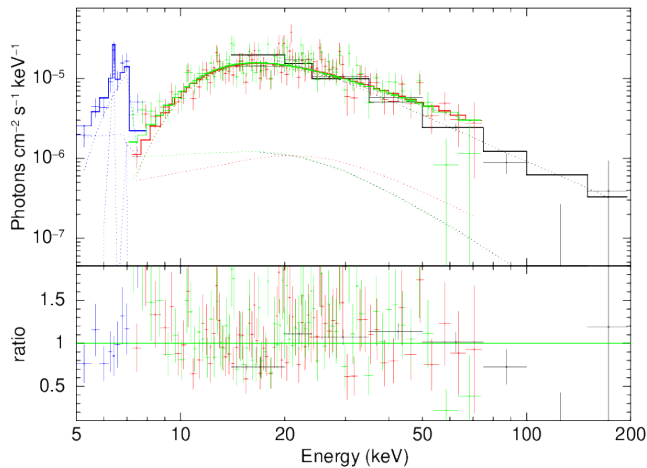


Figure 11. NGC 3079 X-ray spectrum CXO data in blue, NuSTAR FMPA/FPMB data in red and green, and BAT data in black. The angular resolution of CXO has allowed us to confine the AGN emission at soft X-ray energies and fit the Fe $K\alpha$ line, and the sensitivity of NuSTAR has allowed us to obtain a more precise estimate of N_{H} .

the spectral index corresponding to the CXO data to vary we find that this fit produces an unusually hard spectral index of $\Gamma_{\text{CXO}} = 0.9^{+0.5}_{-0.4}$, which given the uncertainties may be due to the relative insensitivity of the CXO data to the intrinsic power-law continuum in the presence of heavy absorption. Tying Γ to the best-fit value of the BAT data group $\Gamma = 1.96$ is disfavored by an F -test, which gives $p = 1.5 \times 10^{-3}$. Setting Γ_{CXO} to the 90% upper confidence limit of 1.4 gives $\chi^2/\text{dof} = 144.71/142$ and $N_{\text{H}} = 6.1^{+0.4}_{-0.3} \times 10^{23} \text{ cm}^{-2}$, within 0.2 and 0.1 dex of the values respectively reported in [Eguchi et al. \(2011\)](#) and [Ricci et al. \(2017\)](#). We show the best-fit spectrum in [Figure 14](#)

NGC 4151

The X-ray spectrum of NGC 4151 is known to be complex, containing a rich array of emission lines at soft ($< 1 \text{ keV}$) energies (e.g., [Schurch et al. 2004](#)), as well as significant spectral variation (e.g., [Zoghbi et al. 2019](#)). The BAT spectrum exhibits downward curvature at the highest energies suggestive of reflection, and we initially fit the BAT spectrum

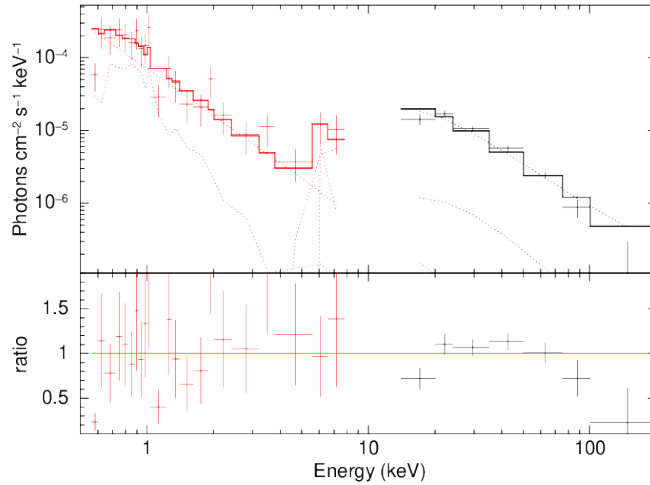


Figure 12. NGC 3079 X-ray spectrum with contemporaneous XRT data in red and BAT 105-month data in black.

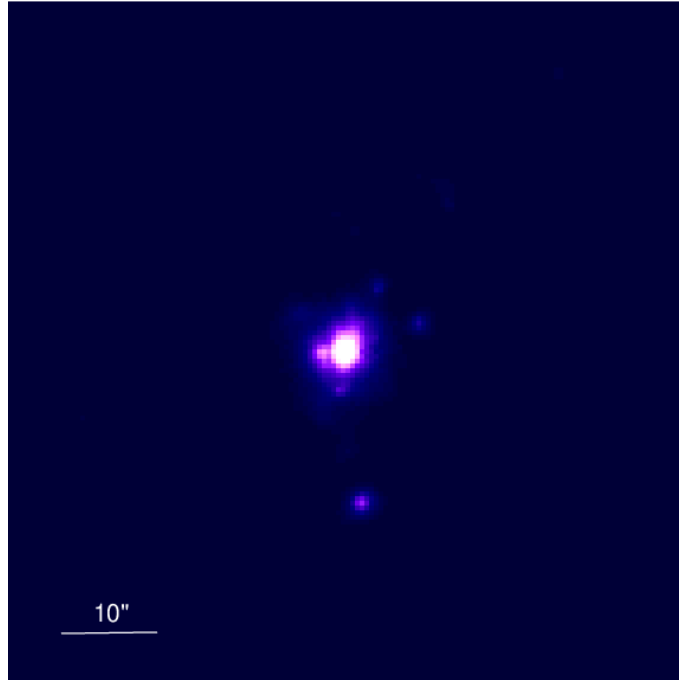


Figure 13. NGC 3081 CXO 0.5–10 keV image (adaptively smoothed). The VLA C-band contours lie entirely within the bright central source and so have been omitted.

with the exponentially cut off power-law reflection model `pexrav` (Magdziarz & Zdziarski 1995). Holding the best-fit parameters fixed, we added the XRT data and appended the partial covering, partially ionized absorber component `zxcipcf` as was used for NGC 4151 in Lubiński et al. (2016). To account for unresolved line emission below < 1 keV, we appended a simple black body component, but we do not attribute to its best-fit parameters any physical significance. We found that the fit is insensitive to the reflection scaling factor, with the best-fit value being statistically consistent with zero. We therefore replaced the `pexrav` component with a power-law with a high energy cutoff (`zcutoffpl`). The best-fit parameters yield $N_{\text{H}} = 1.9^{+0.4}_{-1.3} \times 10^{23} \text{ cm}^{-2}$ and $\Gamma = 1.54^{+0.04}_{-0.04}$.

NGC 4180

One CXO observation exists for this object (Obs ID 9438; 2008 November 16; PI: Walter), but the object is exceptionally faint, with only 8 counts within a $1''.5$ aperture centered on the AGN. Using an archival NuSTAR observation (Obs ID 60201038002), we performed a joint fit with the BAT 105-month spectrum using MYTorus.

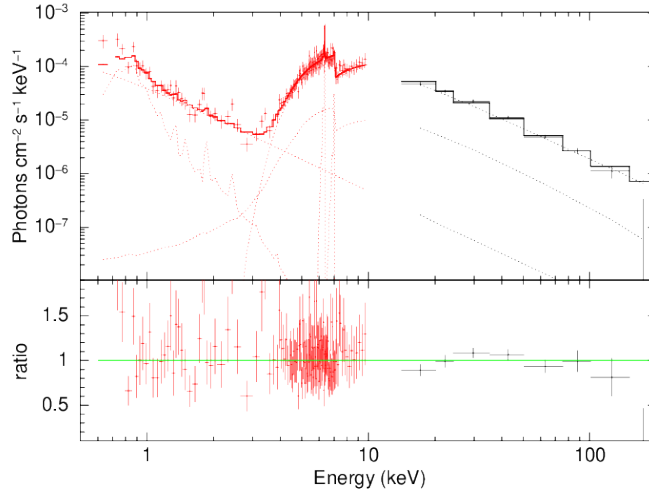


Figure 14. NGC 3081 X-ray spectrum with CXO data in red and BAT 105-month data in black.

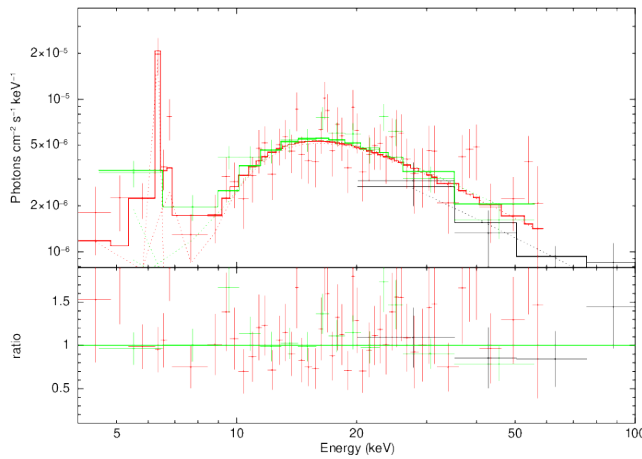


Figure 15. NGC 4180 X-ray spectrum with NuSTAR FPMA/FPMB (red/green) and BAT (black) data.

We find an excellent fit ($\chi^2/\text{dof} = 107.31/107$ with $N_{\text{H}} = 7.3^{+1.7}_{-1.5} \times 10^{24} \text{ cm}^{-2}$, indicating that NGC 4180 is a bona fide Compton-thick AGN. We note that this result is somewhat in tension with Ricci et al. (2017), who find $N_{\text{H}} = 1.4^{+0.6}_{-0.6} \times 10^{24} \text{ cm}^{-2}$ using a more phenomenological model and BAT 70-month catalog data (Baumgartner et al. 2013). We show the best-fit spectrum in Figure 15.

NGC 5506

As with NGC 4151, a downward spectral curvature at high energies is present in the X-ray spectrum of NGC 5506, suggesting reflection or a high energy cutoff, and a partially ionized X-ray absorber is more consistent with the data than a simple photoelectric absorption model (i.e., `phabs`). However, unlike NGC 4151 we find that the BAT spectrum is significantly better fit with a `pexrav` reflection model than a `zcutoffpl` cutoff power-law model ($\chi^2_{\nu} = 0.44$ versus 3.5), and the latter yields an unusually hard spectral index of $\Gamma = 0.8$ while the former yields $\Gamma = 1.8$.

NGC 7378

The contemporaneous XRT data for this object, ObsID 00088600003, is exceptionally faint, with only 5 spectral data counts. Consequently, the XRT and BAT data do not preclude the possibility that this source is Compton-thick, and a naive fit using the MYTorus model gives $N_{\text{H}} \sim 3 \times 10^{24} \text{ cm}^{-2}$, with a 90% confidence lower limit of $2 \times 10^{23} \text{ cm}^{-2}$ and the upper limit pegged at 10^{25} cm^{-2} . To resolve this ambiguity, we used archival NuSTAR (Harrison et al. 2013) FPMA, FPMB data of NGC 7378, ObsID 60464202002 (2018 December 22; 20.3 ks; PI: Harrison), taken as part of

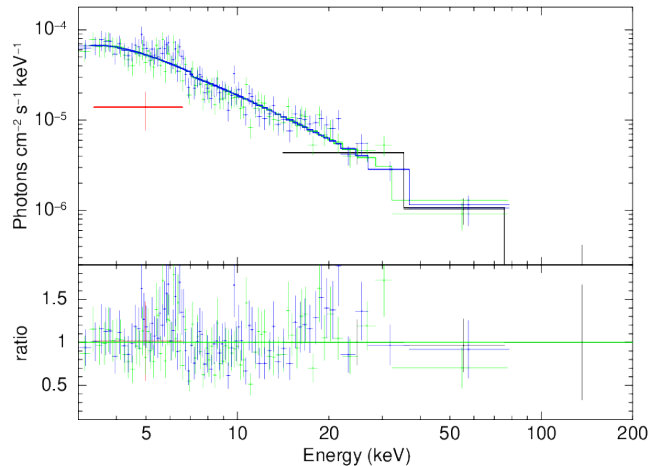


Figure 16. NGC 7378 X-ray spectrum with contemporaneous XRT data in red, BAT 105-month data in black, and NuSTAR FPMA/FPMB in green and blue, respectively. The XRT data are significantly fainter than the BAT/NuSTAR data, indicating potential variability at soft X-rays.

the NuSTAR extragalactic surveys (Harrison et al. 2016), for which we extracted data products using the interactive analysis feature on the Space Science Data Center website.⁹

After including the NuSTAR data, we find that the X-ray spectrum of NGC 7378 is well-described by an absorbed power-law with $N_{\text{H}} = 5.8^{+2.2}_{-2.1} \times 10^{22} \text{ cm}^{-2}$ and $\Gamma = 1.7^{+0.1}_{-0.1}$. The model normalizations of the power-law fits to the BAT and NuSTAR data are consistent with a $\sim 10\%$ instrumental calibration uncertainty; however the power-law normalization of the XRT data is considerably lower, being $\sim 26\%$ of the value of the NuSTAR data normalization (Figure 16), with a 90% upper limit of 54%. This indicates potential variability between the NuSTAR and XRT epochs, which are separated by 4.5 months, and so we calculate the 2–10 keV flux corresponding to the XRT data normalization while holding the other spectral parameters to the values determined from the fit to all four datasets.

NGC 7479

This object is listed as borderline Compton-thick ($N_{\text{H}} = 1.4 \times 10^{24} \text{ cm}^{-2}$) by Ricci et al. (2017). We reprocessed an archival NuSTAR observation (Obs ID 60201037002; 2016 May 12; PI: Ricci) of NGC 7479 and jointly fit its BAT 105-month data using MYTorus above 3 keV, finding an excellent fit ($\chi^2/\text{dof} = 76.99/77$) with $\Gamma = 2.47^{+0.12}_{-0.11}$ and $N_{\text{H}} = 5.7^{+0.5}_{-0.5} \times 10^{24} \text{ cm}^{-2}$, for a torus inclination angle of $\theta = 79^\circ$, where 0° is face-on. NGC 7479 is therefore fully Compton-thick, and we do not expect our XRT observations to have any sensitivity to the intrinsic power-law continuum. However, we briefly explore the soft X-ray properties of this object by downloading and reprocessing an archival CXO observation (Obs ID 11230; 2009 August 11; PI: Pooley). The high resolution CXO observation reveals extensive diffuse emission near the AGN, as shown in Figure 17. We extract the soft X-ray spectrum using an aperture matched to that of NuSTAR. We find that the joint CXO, NuSTAR, and BAT spectrum is well-fit ($\chi^2/\text{dof} = 151.04/134$ with the addition of a single APEC plasma component with $kT = 0.7 \text{ keV}$). The intrinsic power-law spectral index and column density are not significantly affected by the addition of the CXO data, although curiously the relative normalization of the Fe $K\alpha$ line in the CXO data is required to be ~ 4 times higher than in the other data. We show the fit to the full X-ray spectrum in Figure 18.

REFERENCES

- Anders, E., & Grevesse, N. 1989, *GeoCoA*, 53, 197,
doi: [10.1016/0016-7037\(89\)90286-X](https://doi.org/10.1016/0016-7037(89)90286-X)
- Arnaud, K. A. 1996, in *Astronomical Society of the Pacific Conference Series*, Vol. 101, *Astronomical Data Analysis Software and Systems V*, ed. G. H. Jacoby & J. Barnes,

⁹ <http://nustar.ssdsc.asi.it>

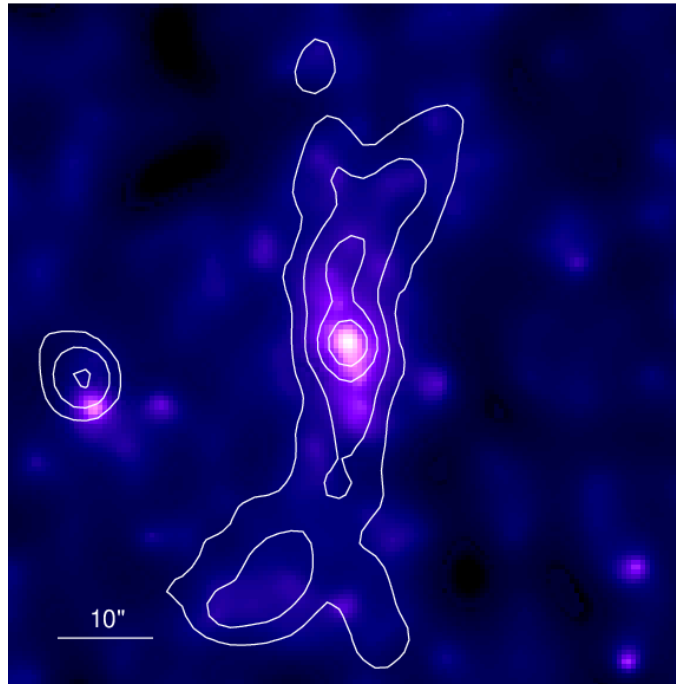


Figure 17. NGC 7479 CXO 0.5–10 keV image (adaptively smoothed). For reference we also include C-band (6 GHz) contours from an archival C/C-configuration VLA observation, showing the extended radio morphology coinciding with diffuse soft X-rays emission.

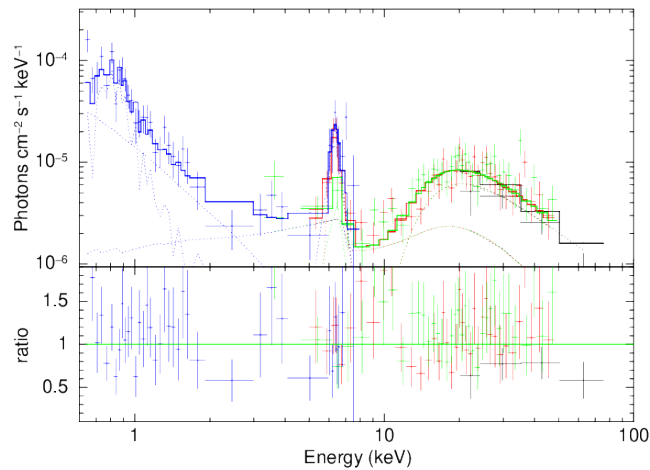


Figure 18. NGC 7479 X-ray spectrum.

Assafin, M., Vieira-Martins, R., Andrei, A. H., Camargo, J. I. B., & da Silva Neto, D. N. 2013, *MNRAS*, 430, 2797, doi: [10.1093/mnras/stt081](https://doi.org/10.1093/mnras/stt081)

Astropy Collaboration, Robitaille, T. P., Tollerud, E. J., et al. 2013, *A&A*, 558, A33, doi: [10.1051/0004-6361/201322068](https://doi.org/10.1051/0004-6361/201322068)

Bañados, E., Venemans, B. P., Mazzucchelli, C., et al. 2018, *Nature*, 553, 473, doi: [10.1038/nature25180](https://doi.org/10.1038/nature25180)

Baek, J., Chung, A., Schawinski, K., et al. 2019, *MNRAS*, 488, 4317, doi: [10.1093/mnras/stz1995](https://doi.org/10.1093/mnras/stz1995)

Bär, R. E., Trakhtenbrot, B., Oh, K., et al. 2019, *MNRAS*, 489, 3073, doi: [10.1093/mnras/stz2309](https://doi.org/10.1093/mnras/stz2309)

Baumgartner, W. H., Tueller, J., Markwardt, C. B., et al. 2013, *ApJS*, 207, 19, doi: [10.1088/0067-0049/207/2/19](https://doi.org/10.1088/0067-0049/207/2/19)

Blakeslee, J. P., Lucey, J. R., Barris, B. J., Hudson, M. J., & Tonry, J. L. 2001, *MNRAS*, 327, 1004, doi: [10.1046/j.1365-8711.2001.04800.x](https://doi.org/10.1046/j.1365-8711.2001.04800.x)

Burrows, D. N., Hill, J. E., Nousek, J. A., et al. 2003, in *Society of Photo-Optical Instrumentation Engineers (SPIE) Conference Series*, Vol. 4851, Proc. SPIE, ed. J. E. Truemper & H. D. Tananbaum, 1320–1325, doi: [10.1117/12.461279](https://doi.org/10.1117/12.461279)

Burrows, D. N., Hill, J. E., Nousek, J. A., et al. 2005, *SSRv*, 120, 165, doi: [10.1007/s11214-005-5097-2](https://doi.org/10.1007/s11214-005-5097-2)

- Calzetti, D., Armus, L., Bohlin, R. C., et al. 2000, *ApJ*, 533, 682, doi: [10.1086/308692](https://doi.org/10.1086/308692)
- Condon, J. J. 1992, *ARA&A*, 30, 575, doi: [10.1146/annurev.aa.30.090192.003043](https://doi.org/10.1146/annurev.aa.30.090192.003043)
- da Silva Neto, D. N., Andrei, A. H., Vieira Martins, R., & Assafin, M. 2002, *AJ*, 124, 612, doi: [10.1086/341163](https://doi.org/10.1086/341163)
- de Grijp, M. H. K., Keel, W. C., Miley, G. K., Goudfrooij, P., & Lub, J. 1992, *A&AS*, 96, 389
- de Vaucouleurs, G., & Olson, D. W. 1984, *ApJS*, 56, 91, doi: [10.1086/190977](https://doi.org/10.1086/190977)
- Dorland, B., Secrest, N., Johnson, M., et al. 2020, arXiv e-prints, arXiv:2009.02169. <https://arxiv.org/abs/2009.02169>
- Eguchi, S., Ueda, Y., Awaki, H., et al. 2011, *ApJ*, 729, 31, doi: [10.1088/0004-637X/729/1/31](https://doi.org/10.1088/0004-637X/729/1/31)
- Evans, P. A., Beardmore, A. P., Page, K. L., et al. 2009, *MNRAS*, 397, 1177, doi: [10.1111/j.1365-2966.2009.14913.x](https://doi.org/10.1111/j.1365-2966.2009.14913.x)
- Ferrarese, L., & Merritt, D. 2000, *ApJL*, 539, L9, doi: [10.1086/312838](https://doi.org/10.1086/312838)
- Fey, A. L., Gordon, D., Jacobs, C. S., et al. 2015, *AJ*, 150, 58, doi: [10.1088/0004-6256/150/2/58](https://doi.org/10.1088/0004-6256/150/2/58)
- Gallimore, J. F., Baum, S. A., & O’Dea, C. P. 1997, *Nature*, 388, 852, doi: [10.1038/42201](https://doi.org/10.1038/42201)
- . 2004, *ApJ*, 613, 794, doi: [10.1086/423167](https://doi.org/10.1086/423167)
- Gallo, E., Miller, B. P., & Fender, R. 2012, *MNRAS*, 423, 590, doi: [10.1111/j.1365-2966.2012.20899.x](https://doi.org/10.1111/j.1365-2966.2012.20899.x)
- Gebhardt, K., Bender, R., Bower, G., et al. 2000, *ApJL*, 539, L13, doi: [10.1086/312840](https://doi.org/10.1086/312840)
- Gültekin, K., Cackett, E. M., Miller, J. M., et al. 2009, *ApJ*, 706, 404, doi: [10.1088/0004-637X/706/1/404](https://doi.org/10.1088/0004-637X/706/1/404)
- Harris, H. C., Dahn, C. C., Zacharias, N., et al. 2016, *AJ*, 152, 118, doi: [10.3847/0004-6256/152/5/118](https://doi.org/10.3847/0004-6256/152/5/118)
- Harrison, F. A., Craig, W. W., Christensen, F. E., et al. 2013, *ApJ*, 770, 103, doi: [10.1088/0004-637X/770/2/103](https://doi.org/10.1088/0004-637X/770/2/103)
- Harrison, F. A., Aird, J., Civano, F., et al. 2016, *ApJ*, 831, 185, doi: [10.3847/0004-637X/831/2/185](https://doi.org/10.3847/0004-637X/831/2/185)
- Herrera Ruiz, N., Middelberg, E., Deller, A., et al. 2017, *A&A*, 607, A132, doi: [10.1051/0004-6361/201731163](https://doi.org/10.1051/0004-6361/201731163)
- . 2018, *A&A*, 616, A128, doi: [10.1051/0004-6361/201832969](https://doi.org/10.1051/0004-6361/201832969)
- Hill, J. E., Burrows, D. N., Nousek, J. A., et al. 2004, in *Society of Photo-Optical Instrumentation Engineers (SPIE) Conference Series*, Vol. 5165, Proc. SPIE, ed. K. A. Flanagan & O. H. W. Siegmund, 217–231, doi: [10.1117/12.505728](https://doi.org/10.1117/12.505728)
- Ho, L. C., Filippenko, A. V., & Sargent, W. L. W. 1997, *ApJS*, 112, 315, doi: [10.1086/313041](https://doi.org/10.1086/313041)
- Hönig, S. F., Watson, D., Kishimoto, M., & Hjorth, J. 2014, *Nature*, 515, 528, doi: [10.1038/nature13914](https://doi.org/10.1038/nature13914)
- Kennicutt, Robert C., J. 1998, *ARA&A*, 36, 189, doi: [10.1146/annurev.astro.36.1.189](https://doi.org/10.1146/annurev.astro.36.1.189)
- Kormendy, J., & Ho, L. C. 2013, *ARA&A*, 51, 511, doi: [10.1146/annurev-astro-082708-101811](https://doi.org/10.1146/annurev-astro-082708-101811)
- Koshida, S., Yoshii, Y., Kobayashi, Y., et al. 2017, *ApJL*, 842, L13, doi: [10.3847/2041-8213/aa7553](https://doi.org/10.3847/2041-8213/aa7553)
- Koss, M., Trakhtenbrot, B., Ricci, C., et al. 2017, *ApJ*, 850, 74, doi: [10.3847/1538-4357/aa8ec9](https://doi.org/10.3847/1538-4357/aa8ec9)
- Koss, M. J., Assef, R., Baloković, M., et al. 2016, *ApJ*, 825, 85, doi: [10.3847/0004-637X/825/2/85](https://doi.org/10.3847/0004-637X/825/2/85)
- Kovalev, Y. Y., Petrov, L., & Plavin, A. V. 2017, *A&A*, 598, L1, doi: [10.1051/0004-6361/201630031](https://doi.org/10.1051/0004-6361/201630031)
- LaMassa, S. M., Yaqoob, T., Boorman, P. G., et al. 2019, *ApJ*, 887, 173, doi: [10.3847/1538-4357/ab552c](https://doi.org/10.3847/1538-4357/ab552c)
- Laor, A., & Behar, E. 2008, *MNRAS*, 390, 847, doi: [10.1111/j.1365-2966.2008.13806.x](https://doi.org/10.1111/j.1365-2966.2008.13806.x)
- Lavalley, M., Isobe, T., & Feigelson, E. 1992, in *Astronomical Society of the Pacific Conference Series*, Vol. 25, *Astronomical Data Analysis Software and Systems I*, ed. D. M. Worrall, C. Biemesderfer, & J. Barnes, 245
- Leitherer, C., Schaerer, D., Goldader, J. D., et al. 1999, *ApJS*, 123, 3, doi: [10.1086/313233](https://doi.org/10.1086/313233)
- Li, J.-T., Hodges-Kluck, E., Stein, Y., et al. 2019, *ApJ*, 873, 27, doi: [10.3847/1538-4357/ab010a](https://doi.org/10.3847/1538-4357/ab010a)
- Lister, M. L., Homan, D. C., Hovatta, T., et al. 2019, *ApJ*, 874, 43, doi: [10.3847/1538-4357/ab08ee](https://doi.org/10.3847/1538-4357/ab08ee)
- Lubiński, P., Beckmann, V., Gibaud, L., et al. 2016, *MNRAS*, 458, 2454, doi: [10.1093/mnras/stw454](https://doi.org/10.1093/mnras/stw454)
- Ma, C., Arias, E. F., Eubanks, T. M., et al. 1998, *AJ*, 116, 516, doi: [10.1086/300408](https://doi.org/10.1086/300408)
- Magdziarz, P., & Zdziarski, A. A. 1995, *MNRAS*, 273, 837, doi: [10.1093/mnras/273.3.837](https://doi.org/10.1093/mnras/273.3.837)
- Makarov, V. V., Frouard, J., Berghea, C. T., et al. 2017, *ApJL*, 835, L30, doi: [10.3847/2041-8213/835/2/L30](https://doi.org/10.3847/2041-8213/835/2/L30)
- McMullin, J. P., Waters, B., Schiebel, D., Young, W., & Golap, K. 2007, in *Astronomical Society of the Pacific Conference Series*, Vol. 376, *Astronomical Data Analysis Software and Systems XVI*, ed. R. A. Shaw, F. Hill, & D. J. Bell, 127
- Merloni, A., Heinz, S., & di Matteo, T. 2003, *MNRAS*, 345, 1057, doi: [10.1046/j.1365-2966.2003.07017.x](https://doi.org/10.1046/j.1365-2966.2003.07017.x)
- Middelberg, E., Deller, A. T., Norris, R. P., et al. 2013, *A&A*, 551, A97, doi: [10.1051/0004-6361/201220374](https://doi.org/10.1051/0004-6361/201220374)
- Moustakas, J., & Kennicutt, Robert C., J. 2006, *ApJS*, 164, 81, doi: [10.1086/500971](https://doi.org/10.1086/500971)
- Murphy, K. D., & Yaqoob, T. 2009, *MNRAS*, 397, 1549, doi: [10.1111/j.1365-2966.2009.15025.x](https://doi.org/10.1111/j.1365-2966.2009.15025.x)
- Netzer, H. 2015, *ARA&A*, 53, 365, doi: [10.1146/annurev-astro-082214-122302](https://doi.org/10.1146/annurev-astro-082214-122302)

- Oh, K., Koss, M., Markwardt, C. B., et al. 2018, *ApJS*, 235, 4, doi: [10.3847/1538-4365/aaa7fd](https://doi.org/10.3847/1538-4365/aaa7fd)
- Orosz, G., & Frey, S. 2013, *A&A*, 553, A13, doi: [10.1051/0004-6361/201321279](https://doi.org/10.1051/0004-6361/201321279)
- Panessa, F., Baldi, R. D., Laor, A., et al. 2019, *Nature Astronomy*, 3, 387, doi: [10.1038/s41550-019-0765-4](https://doi.org/10.1038/s41550-019-0765-4)
- Panessa, F., & Giroletti, M. 2013, *MNRAS*, 432, 1138, doi: [10.1093/mnras/stt547](https://doi.org/10.1093/mnras/stt547)
- Pedreros, M., & Madore, B. F. 1981, *ApJS*, 45, 541, doi: [10.1086/190724](https://doi.org/10.1086/190724)
- Petrov, L., Kovalev, Y. Y., & Plavin, A. V. 2019, *MNRAS*, 482, 3023, doi: [10.1093/mnras/sty2807](https://doi.org/10.1093/mnras/sty2807)
- Plavin, A. V., Kovalev, Y. Y., & Petrov, L. Y. 2019, *ApJ*, 871, 143, doi: [10.3847/1538-4357/aaf650](https://doi.org/10.3847/1538-4357/aaf650)
- Powell, M. C., Cappelluti, N., Urry, C. M., et al. 2018, *ApJ*, 858, 110, doi: [10.3847/1538-4357/aabd7f](https://doi.org/10.3847/1538-4357/aabd7f)
- Reis, R. C., & Miller, J. M. 2013, *ApJL*, 769, L7, doi: [10.1088/2041-8205/769/1/L7](https://doi.org/10.1088/2041-8205/769/1/L7)
- Ricci, C., Trakhtenbrot, B., Koss, M. J., et al. 2017, *ApJS*, 233, 17, doi: [10.3847/1538-4365/aa96ad](https://doi.org/10.3847/1538-4365/aa96ad)
- Robitaille, T., & Bressert, E. 2012, *APLpy: Astronomical Plotting Library in Python*. <http://ascl.net/1208.017>
- Salpeter, E. E. 1955, *ApJ*, 121, 161, doi: [10.1086/145971](https://doi.org/10.1086/145971)
- Schurch, N. J., Warwick, R. S., Griffiths, R. E., & Kahn, S. M. 2004, *MNRAS*, 350, 1, doi: [10.1111/j.1365-2966.2004.07632.x](https://doi.org/10.1111/j.1365-2966.2004.07632.x)
- Shimizu, T. T., Davies, R. I., Koss, M., et al. 2018, *ApJ*, 856, 154, doi: [10.3847/1538-4357/aab09e](https://doi.org/10.3847/1538-4357/aab09e)
- Singal, A. K. 2019, *MNRAS*, 488, L104, doi: [10.1093/mnrasl/slz107](https://doi.org/10.1093/mnrasl/slz107)
- Smith, K. L., Mushotzky, R. F., Koss, M., et al. 2020, *MNRAS*, 492, 4216, doi: [10.1093/mnras/stz3608](https://doi.org/10.1093/mnras/stz3608)
- Smith, R. K., Brickhouse, N. S., Liedahl, D. A., & Raymond, J. C. 2001, *ApJL*, 556, L91, doi: [10.1086/322992](https://doi.org/10.1086/322992)
- Sofue, Y. 1991, *PASJ*, 43, 671
- Terashima, Y., & Wilson, A. S. 2003, *ApJ*, 583, 145, doi: [10.1086/345339](https://doi.org/10.1086/345339)
- Terry, J. N., Paturol, G., & Ekholm, T. 2002, *A&A*, 393, 57, doi: [10.1051/0004-6361:20021018](https://doi.org/10.1051/0004-6361:20021018)
- Trakhtenbrot, B., Ricci, C., Koss, M. J., et al. 2017, *MNRAS*, 470, 800, doi: [10.1093/mnras/stx1117](https://doi.org/10.1093/mnras/stx1117)
- Tueller, J., Baumgartner, W. H., Markwardt, C. B., et al. 2010, *ApJS*, 186, 378, doi: [10.1088/0067-0049/186/2/378](https://doi.org/10.1088/0067-0049/186/2/378)
- Tully, R. B., Courtois, H. M., & Sorce, J. G. 2016, *AJ*, 152, 50, doi: [10.3847/0004-6256/152/2/50](https://doi.org/10.3847/0004-6256/152/2/50)
- Tully, R. B., & Fisher, J. R. 1988, *Catalog of Nearby Galaxies*
- Tully, R. B., Courtois, H. M., Dolphin, A. E., et al. 2013, *AJ*, 146, 86, doi: [10.1088/0004-6256/146/4/86](https://doi.org/10.1088/0004-6256/146/4/86)
- Tzanavaris, P., & Georgantopoulos, I. 2007, *A&A*, 468, 129, doi: [10.1051/0004-6361:20066370](https://doi.org/10.1051/0004-6361:20066370)
- van Moorsel, G., Kembell, A., & Greisen, E. 1996, in *Astronomical Society of the Pacific Conference Series*, Vol. 101, *Astronomical Data Analysis Software and Systems V*, ed. G. H. Jacoby & J. Barnes, 37
- Verner, D. A., Ferland, G. J., Korista, K. T., & Yakovlev, D. G. 1996, *ApJ*, 465, 487, doi: [10.1086/177435](https://doi.org/10.1086/177435)
- Volonteri, M. 2010, *A&A Rv*, 18, 279, doi: [10.1007/s00159-010-0029-x](https://doi.org/10.1007/s00159-010-0029-x)
- Willick, J. A., Courteau, S., Faber, S. M., et al. 1997, *ApJS*, 109, 333, doi: [10.1086/312983](https://doi.org/10.1086/312983)
- Willingale, R., Starling, R. L. C., Beardmore, A. P., Tanvir, N. R., & O'Brien, P. T. 2013, *MNRAS*, 431, 394, doi: [10.1093/mnras/stt175](https://doi.org/10.1093/mnras/stt175)
- Zacharias, N., & Zacharias, M. I. 2014, *AJ*, 147, 95, doi: [10.1088/0004-6256/147/5/95](https://doi.org/10.1088/0004-6256/147/5/95)
- Zakamska, N. L., & Greene, J. E. 2014, *MNRAS*, 442, 784, doi: [10.1093/mnras/stu842](https://doi.org/10.1093/mnras/stu842)
- Zhang, J. S., Henkel, C., Kadler, M., et al. 2006, *A&A*, 450, 933, doi: [10.1051/0004-6361:20054138](https://doi.org/10.1051/0004-6361:20054138)
- Zoghbi, A., Miller, J. M., & Cackett, E. 2019, *ApJ*, 884, 26, doi: [10.3847/1538-4357/ab3e31](https://doi.org/10.3847/1538-4357/ab3e31)